Technical Memo

905

Superobbing and Finer Thinning for All-sky Humidity Sounder Assimilation

David I. Duncan, Niels Bormann, Alan J. Geer, Peter Weston

March 2023

ECMWF
European Centre for Medium-Range
Weather Forecasts

Abstract

Humidity sounder radiances are currently thinned to about 110 km spacing prior to assimilation at ECMWF and used at native resolution. In this paper, the thinning scale and possible averaging of all-sky humidity sounder observations are considered. Averaging the radiances into "superobs" acts as a low-pass filter and provides smoother images of departures. This decreases effective sensor noise and thus std(O-B), marginally for 183 GHz channels (5-15%) and significantly for 118 GHz channels (5-55%). The method of superobbing is argued to provide more representative observations for assimilation and a better utilisation of total information content than thinning native-resolution radiances, as there is less information discarded prior to assimilation.

Thinning and averaging scales of humidity sounder radiances are investigated separately and then together. Superobbing of humidity sounder radiances and decreased thinning are shown to markedly improve background fits to independent humidity- and wind-sensitive observations, when changed in isolation or in combination. This is indicative of better short-range forecasts of humidity, with winds improved through the 4D-Var tracer effect. Results are relatively insensitive to superob resolution and so it is argued that smaller superobs are preferable for diagnostic purposes. The move from 110 to 70 km thinning provides as much as 140% more radiances for assimilation and much-improved spatial information for diagnostic purposes. These augmentations in the processing of humidity sounder radiances lead to slightly improved wind forecasts in the Southern Hemisphere at medium-range. As part of the upgrade to Cycle 49r1, all-sky humidity sounder radiances will be assimilated at 70 km spacing after being averaged into 50 km superobs.

Plain Language Summary

This report investigates the optimal thinning and averaging scales for humidity sounding microwave observations in the ECMWF assimilation system. The introduction of spatial averaging shows a positive impact, as does assimilation of observations with finer spacing. These changes permit more total information on humidity into the system and both are beneficial for short-range forecasts of humidity and winds in the mid- to upper-troposphere. As the assimilation system and the forecast model move to finer spatial scales in the future, it is important to exploit as much information as possible from these valuable observations.

1 Introduction

All-sky assimilation of cross-track scanning humidity sounder radiances has been operational in the IFS since 2015 (Geer *et al.*, 2014). This covers observations from the Microwave Humidity Sounder (MHS) on several NOAA and Metop platforms and the MicroWave Humidity Sounder 2 (MWHS-2) on the operational FY-3 platforms. These sensors hold multiple channels sampling the strong water vapour absorption feature at 183.31 GHz, providing profile information on the distribution of humidity in the troposphere. The MWHS-2 sensors also provide a mixture of temperature and water vapour information via their 118 GHz channels. Channel details are found in Table 1. As of late 2022, there are three MHS and two MWHS-2 sensors actively assimilated in the IFS, with a third MWHS-2 to be added shortly. Note that MW humidity-sounding information is also assimilated in the IFS from the ATMS instrument, but through a clear-sky approach, and assimilation of this instrument is hence not changed in the present work. Furthermore, the ECMWF system also uses MW humidity-sounding observations from conical scanners like SSMIS and GMI, but given their different observing geometry they are not considered here.

The addition of microwave sounders to the assimilation system has shown consistent benefit for forecast skill in the short- to medium-range (Duncan *et al.*, 2021) when considering temperature and humidity sounders added in tandem. Continued benefit is also seen when adding further humidity sounders (hereafter H-sounders) on their own (Geer *et al.*, 2017b). This has recently been exemplified by the additions of MWHS-2 on FY-3C and FY-3D at ECMWF (Lawrence *et al.*, 2018; Bormann *et al.*, 2021; Duncan and Bormann, 2020), as well as all-sky use of H-sounders in other NWP systems (e.g. Candy and Migliorini, 2021; Carminati and Migliorini, 2021). Much of the benefit is realised via the 4D-Var tracer effect, through which increments in humidity cause adjustments in winds by inference (Peubey and McNally, 2009). In this report we consider addition of H-sounder data by increasing the total volume of information assimilated from existing sensors and platforms. This is accomplished purely by changes to the thinning and averaging of currently available observations.

1.1 Observations

Radiances measured by H-sounders have relatively small FOV sizes compared to other passive microwave sensors, a feature possible because of the shorter wavelengths measured. For example, the 183 GHz channels of MHS have an effective FOV of 16x16 km at nadir compared to 48x48 km for 50 GHz channels on the temperature sounder AMSU-A (Bennartz, 2000). Cross-track sounders have larger FOVs at higher zenith angles (i.e. near scan edge). For example, MHS at scan edge has an FOV of approximately 51x27 km compared to 16x16 km at nadir (Robel and Graumann, 2014). The sampling on the ground is much denser near nadir than at higher zenith angles—see Fig. 1 for an example of FOV sizes across the scan for MWHS-2. A slight difference between MHS and MWHS-2 lies in the wider swath of MWHS-2, enabled by observing out to a greater scan angle (see Table 2). This provides greater spatial coverage for MWHS-2 but does mean that observations at swath edge exhibit an even larger FOV. All MHS and MWHS-2 sensors are on LEO, sun-synchronous satellite platforms.
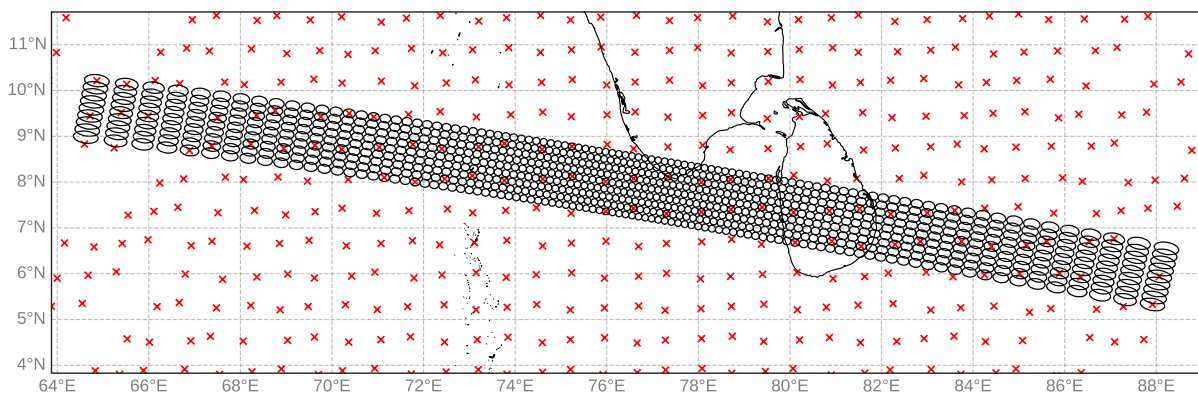

Figure 1: FOVs for 9 consecutive scans (black ovals) and all thinned observation centres at N128 thinning scale (red crosses) for an overpass of MWHS-2 over south India and Sri Lanka.

Sensor noise for assimilated 183 GHz channels varies substantially but is typically in the range of 0.3 to 1.0 K (given by NEDT). Unlike temperature sounding channels, where NWP impact is often limited by the sensor noise due to background errors in temperature on order of 0.1 K, the utility of humidity sounding observations for NWP is not considered noise-limited (Bormann and Bauer, 2010). Background errors at 183 GHz are more of the order 1 K in clear scenes and greater than 2 K with any cloud present. The larger background errors at 183 GHz are in part because of humidity's higher small-scale variability and more significant forward modelling errors because of greater scattering from ice hydrom-

Table 1: Channel numbers, central frequencies, and peak of the weighting functions at nadir for MHS and MWHS-2. Weighting function peaks are quite approximate, as these depend on the atmospheric profile of humidity and also vary with the view angle.

Channel	MHS		MWHS-2	
	Frequency [GHz]	*Peak [hPa]*	*Frequency [GHz]*	*Peak [hPa]*
1	89.0	Surface	89.0	Surface
2	157.0	Surface	118.75±0.08	20
3	183.31±1.0	350	118.75±0.2	60
4	183.31±3.0	500	118.75±0.3	100
5	190.31	650	118.75±0.8	250
6	-	-	118.75±1.1	300
7	-	-	118.75±2.5	700
8	-	-	118.75±3.0	Surface
9	-	-	118.75±5.0	Surface
10	-	-	150.0	Surface
11	-	-	183.31±1.0	350
12	-	-	183.31±1.8	400
13	-	-	183.31±3.0	500
14	-	-	183.31±4.5	550
15	-	-	183.31±7.0	650

Table 2: Scan characteristics for MHS and MWHS-2. FOV sizes are for 183 GHz channels only—118 GHz FOVs on MWHS-2 are larger (32x32 km at nadir) due to a beam width of 2.0 vs. 1.1 ° (He et al., 2014).

Sensor	Swath	Spots per scan	Scan spacing	FOV (nadir)	Max. scan angle
MHS	2180 km	90	16 km	16 x 16 km	49.44 °
MWHS-2	2700 km	98	16 km	16 x 16 km	53.35 °

eteors. In contrast, the 118 GHz sounding channels on MWHS-2 exist on a weaker oxygen absorption line than those near 50 GHz and with relatively thin bandwidths exhibit higher NEDT. As a consequence, the impact of its 118 GHz channels on temperature forecasts has thus far been marginal (Lawrence *et al.*, 2018; Bormann *et al.*, 2021) but may improve with better radiometric performance (Maddy *et al.*, 2022). The other sensitivities of 118 GHz channels—water vapour continuum absorption, cloud water, cloud ice, and precipitation—remain an asset to all-sky assimilation despite the higher NEDT levels.

All 183 GHz channels on MHS and MWHS-2 are actively assimilated in the IFS[1]. The first 5 scan positions for all channels on FY-3C and the first 8 positions for FY-3D channels 13 and 15 are excluded from assimilation due to strong bias characteristics (Lawrence *et al.*, 2018; Duncan and Bormann, 2020), but otherwise the full swath of both sensors is used. On MWHS-2, the 118 GHz channels 2 to 7 are assimilated. The details of which surfaces these channels are assimilated over (as of Cycle 48r1) can be found in Table 3 of Geer *et al.* (2022). Suffice to say that higher-peaking channels are used everywhere, whereas lower-peaking channels like MHS channel 5 or MWHS-2 channels 6 and 7 are used more cautiously over non-ocean surfaces.

---

[1]The only exception is NOAA-19 channel 3, which is not assimilated due to noise levels far outside specification.
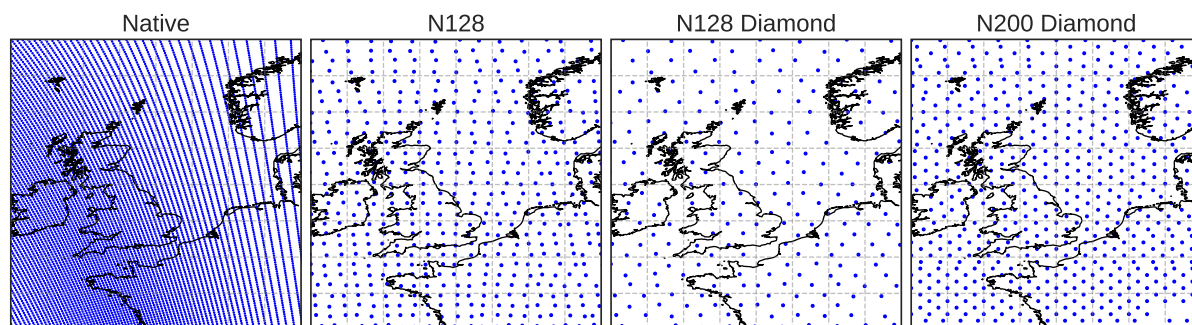
1.2 Thinning and Averaging

Figure 2: MHS observation locations from an overpass of northwestern Europe on 3rd June, 2021. From left to right, panels show observation locations with no thinning applied, N128 thinning, N128 Diamond thinning, and N200 Diamond thinning. Grey lines show 2.5 degree spacing in latitude and longitude.

Satellite radiances are traditionally thinned prior to assimilation. This serves dual purposes: it limits the computational costs involved in processing tens or hundreds of millions of observations and removes observations with potential spatially-correlated observation errors. Thus since the implementation of all-sky H-sounders in the IFS, the first step of observation processing has been to thin the data using a N128[2] Gaussian grid (78 km spacing), selecting the observation nearest to each N128 grid point (shown as crosses in Fig. 1) and discarding all others. This step is visualised by comparing the left two panels of Fig. 2. Note that this thinning requires the observation to lie within 25 km of the Gaussian grid point, so data coverage is sparser near scan edge. A second step of thinning occurs after the first trajectory, selecting every other observation to be thinned out in a diamond pattern, leaving observations at roughly 110 km spacing for the assimilation (compare middle two panels in Fig. 2). The "diamond" pattern thinning discards every other radiance along the row of the grid and then staggers this pattern in the following row; for example, positions 1, 3, and 5 are discarded in row 1, with positions 2, 4, and 6 discarded in row 2, and so on. These observations are at native resolution and not averaged in any way. Figure 2 shows a swath from MHS, contrasting un-thinned observations with three thinning scales.

In contrast, microwave imager radiances are averaged by a process known as "superobbing," a technique used since the early days of direct all-sky radiance assimilation (Geer and Bauer, 2010) to create superobs (super-observations). The transformation of several observations into a single superob serves to homogenise observations from sensors and channels with differing FOVs, whilst making observations more representative of the model grid box they are trying to affect (i.e. treating representation error). The downside of this approach is that finer-scale information is smeared out due to the averaging. At the current version of the IFS (Cycle 48r1), microwave imager radiances are superobbed at N128 resolution and then thinned in a diamond pattern as described above. As stated by Geer *et al.* (2014), "following the logic of the microwave imagers, the MHS observations would ideally have been superobbed, but this has been left for future work."

Comparing the left and centre columns of Fig. 3, we can see the difference between observations thinned and averaged at the same spatial resolution. Each superob is required to contain at least two observations in the grid box but we remove the 25 km requirement of distance from the grid box centre as used in the thinning-only panels, permitting greater data coverage from the superobs at high zenith angles. The superob lat/lon locations are taken from the centre of the grid box rather than the average of the lat/lon values from all points that were used in the superob. The change in noise characteristics for the noise-

---

[2]https://www.ecmwf.int/en/forecasts/documentation-and-support/gaussian_n128

dominated MWHS-2 channel 3 signal is quite stark, revealing striping patterns otherwise not apparent. This effect to reveal striping patterns is most clear for the noise-dominated 118 GHz channels but also seen for Metop-C MHS (not shown). The effect of superobbing also makes certain wave features clearer, such as ripples in O-B in the south Caribbean that appear to be inertia-gravity waves (e.g. O'Sullivan and Dunkerton, 1995). The right column of Fig. 3 shows a finer resolution of superob at N200, about 50 km in the right column vs. 80 km in the centre column. Comparing the two superob resolutions, smaller convective features such as those in the ITCZ are better resolved by the finer superob of the right panels. The smaller N200 superobs may prove useful for diagnostic purposes such as identifying cloud features and misplaced convection at finer scales.
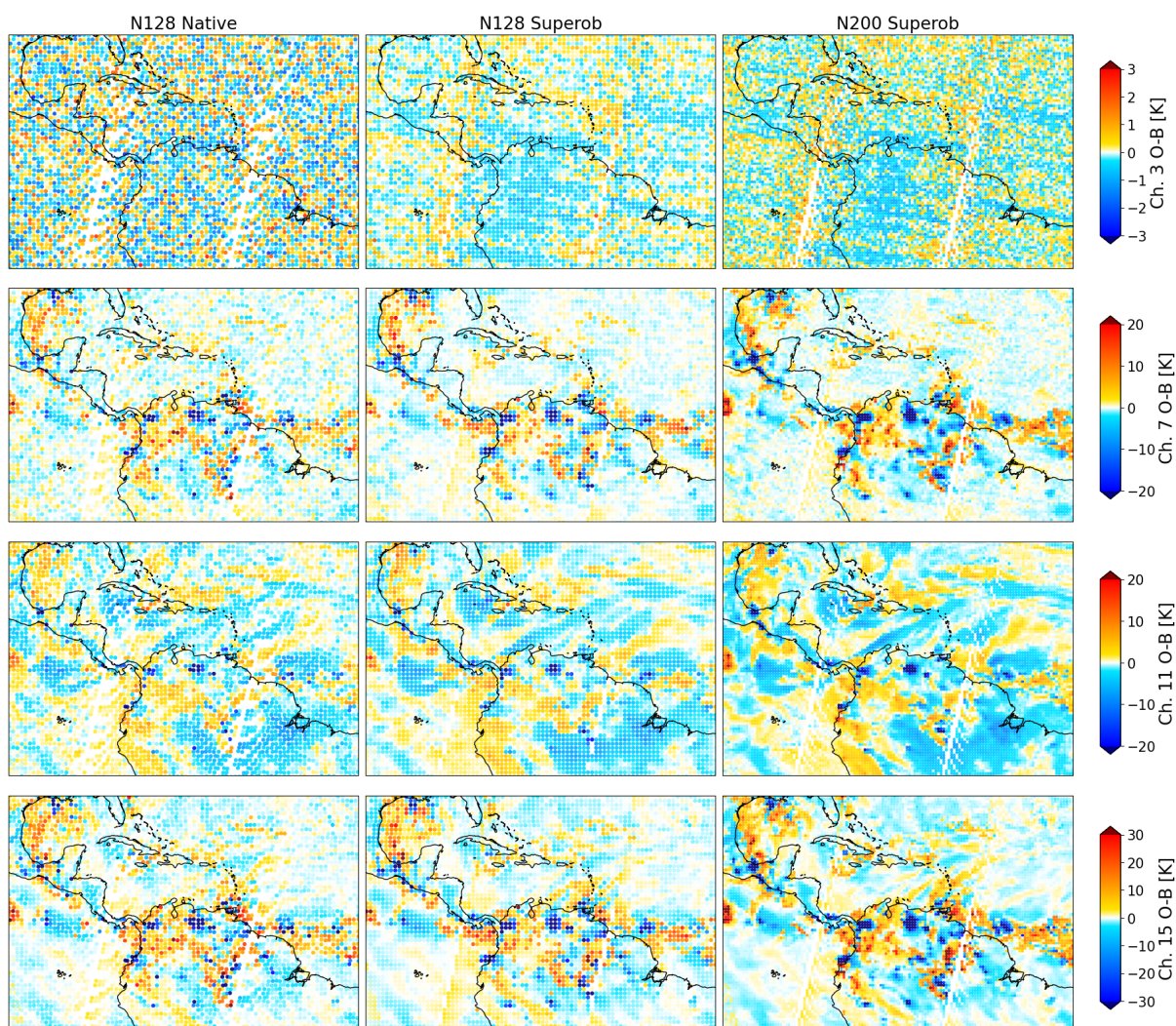

Figure 3: Observations minus background (O-B) over Central America from four channels on FY-3D MWHS-2: 3 (top), 7 (second row), 11 (third row), 15 (bottom). The left column shows radiances at native resolution thinned at N128, middle column is superobbed at N128, right column is superobbed at N200. Data are from the 0Z long window on 5th June, 2021.

1.3 Recent Developments

Some key technical developments in the use of H-sounder radiances have occurred since the all-sky implementation documented by Geer *et al.* (2014), with a few germane to the discussion and thus worth mentioning here. The radiative transfer model used for all-sky microwave sensors, RTTOV-SCATT, was recently refined with significantly improved scattering properties for frozen hydrometeors (Geer *et al.*, 2021) following a parameter estimation approach that selected from modern particle models and different microphysical assumptions (Geer, 2021). This has a large impact on how well 183 GHz observations fit the model, particularly in heavily scattering scenes such as convection over land (Geer *et al.*, 2022). This improvement allowed for the removal of a screening for "excessive" scattering that was used previously for quality control in the first trajectory. Experimentation in this report uses RTTOV-SCATT v13.0 and thus benefits from these advances. In addition, slant-path radiative transfer following Bormann (2017) has recently been extended to H-sounders as part of the Cycle 48r1 upgrade.

Cycle 48r1 also represents an expanded use of all-sky microwave radiances by way of moving towards an "all-surface" capability. This involves several improvements in the treatment of emissivity and mixed-surface scenes while also expanding the use of microwave imager channels at high latitudes and over land (Geer *et al.*, 2022). Regarding H-sounders, these improvements mainly affect the lowest-peaking 183 GHz channels (MHS 5, MWHS-2 14 and 15) which are now assimilated over snow-free land at high latitudes ($> 60 \,°N$) and used more extensively over coastal and mixed (i.e. land/water) scenes. These changes led to a 6-10% increase in H-sounder radiances assimilated globally (see Figs. 19 and 20 in Geer *et al.* (2022) for further detail).

1.4 Total Information Content

The goal of data assimilation could be considered the full, optimal utilisation of all available observational information content to constrain and guide an Earth-System model. In the context of all-sky microwave assimilation, this means exploiting the full spectral and spatial information content of radiances over all surfaces and for all atmospheric conditions. Moving from clear-sky to all-sky assimilation methodology is a key element of realising this goal, as is gradual addition of more spectral information by adding channels that were previously not assimilated. Some of the developments described above regarding mixed scenes and surface emissivity are part of a larger strategy to assimilate microwave radiances more widely over all surfaces.

To illustrate the challenge of using all available information content, we can revisit the example of Fig. 1. If we view all observations from a humidity sounder and also consider spatial variations across the scan (visualising O-B not as dots but as ovals matching the sensor's FOV), we can see how complex the information really is. Figure 4 shows an upper-tropospheric sounding channel. Small gravity wave ripples are visible on the north-south axis near 72E, as is convection east of Sri Lanka with possible cold pools to the east and west, likely misplaced convection out near 87E, and so on. These features span scales up to roughly 300 km. In the figure, crosses mark observations currently ingested into the IFS prior to secondary thinning. Along with Fig. 2, this gives a sense of how much information is discarded by thinning. Quantitatively, as few as 4% of observations are retained near nadir where radiances have 16 km spacing.

In contrast to all-sky usage and better spectral coverage, the spatial aspect of the overall information content from microwave radiances has received less attention. It is common in data assimilation to select a thinning scale that avoids most spatial error correlations. This makes it safer to treat all observation errors as being wholly uncorrelated, guided by studies such as Bormann and Bauer (2010) which found
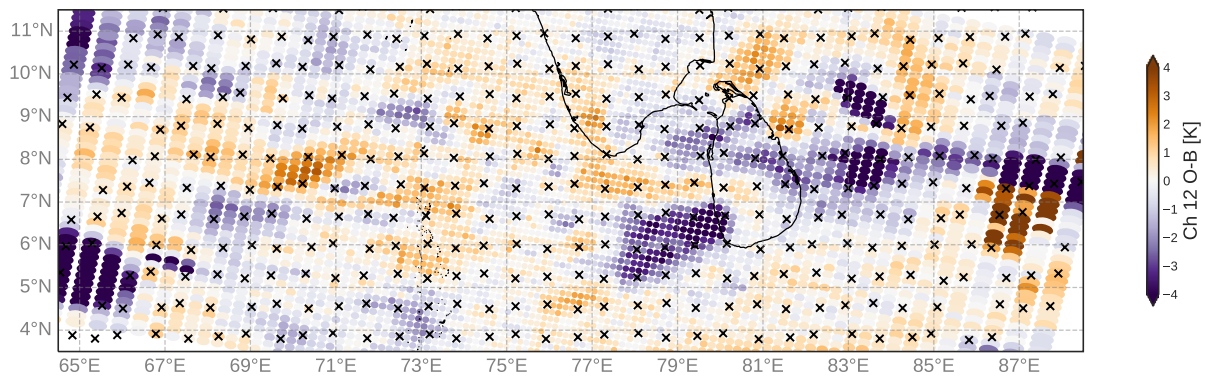
Figure 4: Observations minus background (O-B) near India and Sri Lanka from MWHS-2 channel 12. Each is roughly the shape of the sensor's FOV. Crosses mark the observations ingested into the IFS with current thinning procedures, i.e. passing the N128 thinning as in the 48r1 control experiment.

roughly 80-120 km error correlation scales for MHS radiances in clear-sky. However, error correlations depend on the synoptic conditions, and thus selecting specific situations to use denser observations should hold some benefit (Dando *et al.*, 2007). An example of adaptive thinning can be seen in Kim *et al.* (2020) (their Fig. 14b), with fewer radiances in clear skies and more in areas of cloud and precipitation where correlation lengths are much shorter—all-sky correlation lengths have greater sensitivity to mesoscale meteorology because of the sharper spatial inhomogeneities of clouds and precipitation. As seen in Bonavita *et al.* (2020) (their Fig. 4), upper-tropospheric humidity channels exhibit roughly 100 km error correlation lengths with a maximum of about 200 km in the extratropics at 300 hPa, though shorter scales would be expected if considering tropical convection. Smaller-scale information may be extracted from observations with correlated errors (Bédard and Buehner, 2020), but there is a long-held view that assimilation of observations finer than the error correlation length scale holds little benefit even if correct covariances are assigned (Bergman and Bonner, 1976). In non-theoretical applications where full errors are not prescribed, Hoffman (2018) concludes that "the best strategy is superobservation with a spacing approximately equal to the observation error correlation length scale."

A perfect data assimilation system for radiances would ingest all observations and extract all relevant information content with comprehensive consideration of the inter-channel, spatial, and even time-dependent error correlations. To be clear, none of these is treated explicitly in this paper. Rather, this paper aims to explore the limits of using more radiances in the IFS without resorting to a more complex treatment of such errors. The exploration of finer thinning scales assumes that current thinning may remove more data than is called for by error correlation lengths typical for all-sky humidity radiances. Coupling this with superobbing follows Hoffman (2018), in that the errors assigned are imperfect and do not account for spatial correlations.

2 Method

2.1 Experimental setup

The experiments discussed all use IFS Cycle 48r1 and most cover two seasons: June to August of 2021 and December 2021 to February 2022. This was a time period in which the following H-sounders were

Table 3: Experiment names and characteristics. "Diamond" refers to thinning out every other spot in a diamond pattern. Change in assimilated observations (Δ Obs.) is relative to Control and is an approximate mean across all H-sounder channels given as a percent difference. N-T stands for no-thin. Approximate spacing is the distance between Gaussian grid points for assimilated radiances within the sensor's swath.

	Control (48r1)	**N128 N-T**	**N128 Superob**	**N128 Superob N-T**	**N200 Superob**
Obs. Resolution	Native	Native	78 km	78 km	50 km
Averaging	-	-	Superob	Superob	Superob
1st Thinning	N128	N128	N128	N128	N200
2nd Thinning	Diamond	-	Diamond	-	Diamond
Δ Obs.	-	+100%	+4%	+103%	+137%
Approx. Spacing	110 km	78 km	110 km	78 km	70 km

active: MHS on Metop-A[3], Metop-B, Metop-C, and NOAA-19; MWHS-2 on FY-3C and FY-3D[4]. All experiments use a full observing system that follows that used in ECMWF operations. Final model resolution is at TCo399 (29 km) with 137 vertical levels. The data assimilation uses incremental 4D-Var performed at a final inner loop resolution of TL255 (80 km) with 12-hour delayed cutoff assimilation cycles. Background errors come from the operational EDA (i.e. 47r3, rather than a bespoke 48r1 EDA) due to availability, but this is not expected to significantly alter the results' interpretation (Duncan *et al.*, 2021).

The experiments (Table 3) are analysed in three sets to gauge the impact of the following on H-sounder all-sky assimilation:

- Finer thinning (N128 N-T) – Sec. 3.1

- Superobbing (N128 Superob) – Sec. 3.2

- Superobbing and finer thinning (N128 Superob N-T; N200 Superob) – Sec. 3.3

Additionally, to examine the question of optimal superob resolution, a separate set of experiments was run that covered a shorter time period from late February to late April of 2022. These experiments are listed in Table 4. In these experiments, thinning was tuned to largely conserve the total number of observations assimilated so that the main signal from changing the superob resolution was the resolution change itself rather than the volume of data. Results for this are found in Sec. 3.2.2. It is worth noting that to conserve observation numbers in these particular experiments it is not possible to retain evenly spaced radiances as provided by Gaussian grid thinning and subsequent diamond thinning—the N160 Superob and N256 Superob experiments have unevenly spaced radiances after thinning as a result.

2.2 Observation Error Modelling

Both MHS and MWHS-2 use SI as the cloud proxy (C) in the model for all-sky observation error. SI is the difference of Tb at the 89 and 150 GHz channels ($Tb_1 - Tb_2$ on MHS, $Tb_1 - Tb_{10}$ on MWHS-2), with O the observed Tb after bias correction and B the model background Tb. The full cloud proxy

---

[3]Metop-A de-orbited in November 2021, so was active in only one of the seasons examined.

[4]FY-3D 118 GHz channels (2-7) experienced an anomaly that strongly affected their mean bias in January 2022 and were removed from active assimilation.

Table 4: As Table 3 but change in assimilated observations (Δ Obs.) is relative to N128 Superob. For second thinning, Lon=3 keeps every third longitude point on the grid, Lat=2 keeps every second latitude point, and so on (diamond thinning is equivalent to Lon=2).

	N128 Superob	**N160 Superob**	**N200 Superob**	**N256 Superob**
Obs. Resolution	78 km	62 km	50 km	39 km
Averaging	Superob	Superob	Superob	Superob
1st Thinning	N128	N160	N200	N256
2nd Thinning	Diamond (Lon=2)	Lon=3	Lon=2, Lat=2	Lon=3, Lat=2
Δ Obs.	-	+3%	+17%	+20%

definition is given in Eq. 1 for MHS channel numbers, with the clear-sky difference of Tb subtracted to remove the water vapour signal from SI over sea (see Geer *et al.* (2014), their section 2.4).

$$C_{SI} = ((O_1 - O_2) + (B_1 - B_2))/2 - (B_{clr,1} - B_{clr,2}) \tag{1}$$

SI is sensitive to scattering from ice hydrometeors and precipitation aloft, which is associated with the predominant cause of observation errors at 118 and 183 GHz sounding channels, namely representation errors such as mis-location of convection and difficulties of modelling hydrometeors. This is treated in a "symmetric" fashion that balances observed and model-simulated SI equally (Geer and Bauer, 2011). These observation errors are based on histograms of the standard deviation of O-B as a function of the symmetric SI, and were tuned when the sensors were originally implemented in the IFS (e.g. Geer *et al.*, 2014).
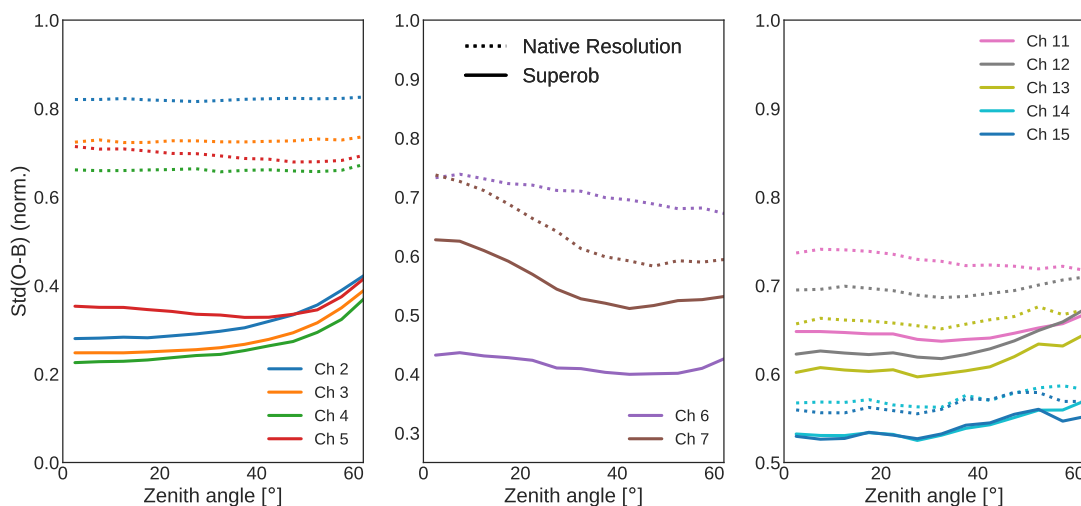

Figure 5: Standard deviation of O-B normalised by the assigned observation errors, given as a function of the zenith angle for assimilated radiances at native resolution (dotted) and N128 superob (solid). Each panel shows different channel groups: 2-5 (left), 6-7 (centre), 11-15 (right). Statistics comprise used data from FY-3D MWHS-2 over sea, August 1-10 2021.

Changes to the thinning alone do not have a large impact on std(O-B) for sounder channels, and thus in these cases there is no need to consider re-tuning the observation error model. However, superobbing H-sounder radiances does prompt consideration of whether the extant error model is sufficient. For expedience and easier interpretation of comparisons between experiments, most of the experiments discussed

here do not modify the observation error models. However, there are significant changes in std(O-B) for noise-dominated channels as a result of superobbing. The higher-peaking 118 GHz channels on MWHS-2 (2-5) witness a large decrease in std(O-B) from superobbing that can be 50% or greater, seen vividly in Fig. 3 for channel 3. Higher-peaking 183 GHz channels also exhibit a decrease in std(O-B), for example about -15% globally for MHS channel 3 when superobbed at N128 resolution. Notably, this change in std(O-B) behaviour is not even across the scan, as more observations are averaged together near nadir and fewer near scan edge, and thus the decrease in noise is most pronounced at low zenith angles; this could perhaps justify a zenith-dependent adjustment to the error model that mirrors what is done for AMSU-A channel 5 (Duncan *et al.*, 2022b, their Fig. 3). One set of experiments explored adjustments to the all-sky observation errors, with these results and discussion found in the Appendix A. These adjustments to the error modelling ultimately did not make much difference to the results and rather highlighted the importance of systematic versus random errors in all-sky error modelling.

Figure 5 shows the interaction between observation error modelling and the choice to superob. Comparison of the dotted and solid lines shows the pure impact of superobbing, as these two experiments used the exact same observation error models. Most noticeable in the plots is the change in magnitude of std(O-B) for MWHS-2 channels 2-6, but the 183 GHz channels also show a shift that is most pronounced for low zenith angles, as much as 12% change for the highest peaking one, channel 11. This indicates that the impact of superobbing on normalised departures differs significantly between channels and for some channels is also as a function of scan position.

3 Results

3.1 Finer thinning

As a first test, we remove the second thinning applied after the first trajectory (see Table 3). This causes a doubling of H-sounder radiances assimilated, with the net spacing changing from roughly 110 to 80 km. The effect of doubling the radiances assimilated has a noticeable impact and can be seen in background departure statistics for various independent observations as shown in Fig. 6. Short-range forecasts of humidity and winds are improved, evidenced in tighter O-B fits of independent observations like GEO infrared radiances and AMVs. The roughly 0.5 to 1% improvement for several infrared and microwave humidity sounding channels is a remarkable signal. To put this in context, the most recent H-sounder activation in the IFS had a smaller impact on these metrics (Duncan and Bormann, 2020). And although ATMS humidity channels are not entirely independent in this context, the improvement for GEO and LEO infrared channels is a similar magnitude and this gives confidence in the signal. Winds are slightly improved at upper tropospheric levels as well, presumably through the 4D-Var tracing effect from better representation of humidity structures (Peubey and McNally, 2009). The only slight degradation seen here is for UTLS temperature channels such as 8-10 on ATMS and equivalent ones on AMSU-A, which is a minor change of about 0.1%. This small degradation is not seen in equivalent IASI or CrIS channels, but may be a consequence of a slightly noisier analysis near the tropopause or weighting the 118 GHz channels too heavily in the analysis.

The changes in medium-range forecast scores for winds and geopotential height are shown in Fig. 7. For most of the scores and time ranges given, the change in forecast scores does not exceed the 95% confidence limits, however the southern hemisphere does appear slightly improved for low-level winds and Z500 RMSE in the medium-range. In contrast, the impact in the northern hemisphere and tropics looks quite neutral.
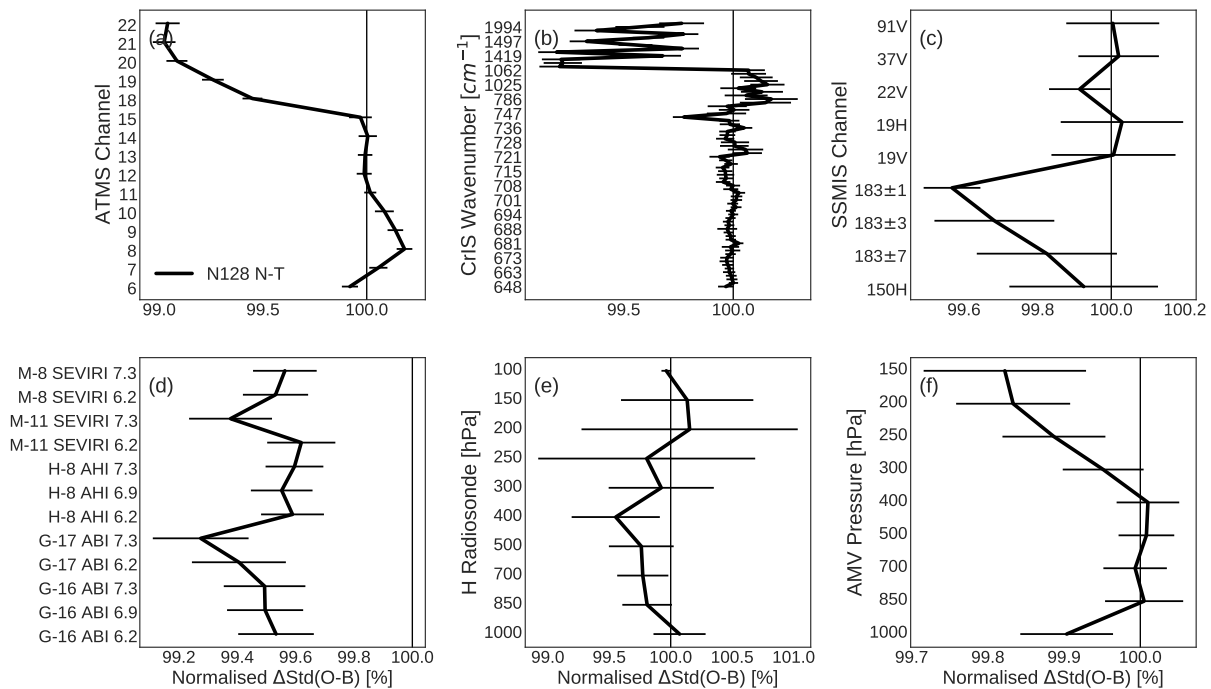
Figure 6: Change in std(O-B) for independent observations caused by the removal of secondary thinning. These include global data from ATMS (a), CrIS (b), SSMIS (c), GEO infrared (d), radiosonde humidity (e), and AMVs (f).

3.2 Superobbing

3.2.1 To Superob or Not

As seen in Fig. 3, superobbing H-sounder observations cleans up the image in some ways that are potentially helpful for diagnostic purposes while allowing more total information to enter the assimilation. However, will a shift to superobbing radiances have any positive effects on the assimilation? To examine this, first we directly compare histograms of observed radiances at different superob resolutions with those from the model background.

The PDF of observed radiances over sea is relatively unaffected by the choice to superob or indeed the superob resolution (Fig. 8). For the most part, it is only at the very cold end of the Tb distribution (below about 220K for MHS channels) that the superob resolution has a noticeable effect, but in these areas coarser averaging helps to bring the observations closer to the model PDF. Interestingly, there are quite rare channel 3 observations greater than 280 K that are almost never seen in the background or superob PDFs; these appear to be observations of small-scale, thick liquid clouds with a very dry free atmosphere above them. The main mismatch between observations and background does not appear to be due to averaging of radiances, but rather systematic under-representation of highly scattering scenes in the model background and too many scenes with moderate levels of scattering, i.e. those about 230-240K for the channels shown. This recalls Geer *et al.* (2017a, their Fig. 16) and Geer and Bauer (2010, their Fig. 14), who showed that the correspondence between PDFs of observed and modelled Tb was relatively poor for a microwave imager at 10 or 19 GHz, regardless of how the observations were averaged together; they pointed to the significance of model bias in simulating clouds, which is a factor that overwhelms the small effect to the PDF caused by superobbing. Geer and Bauer (2010)
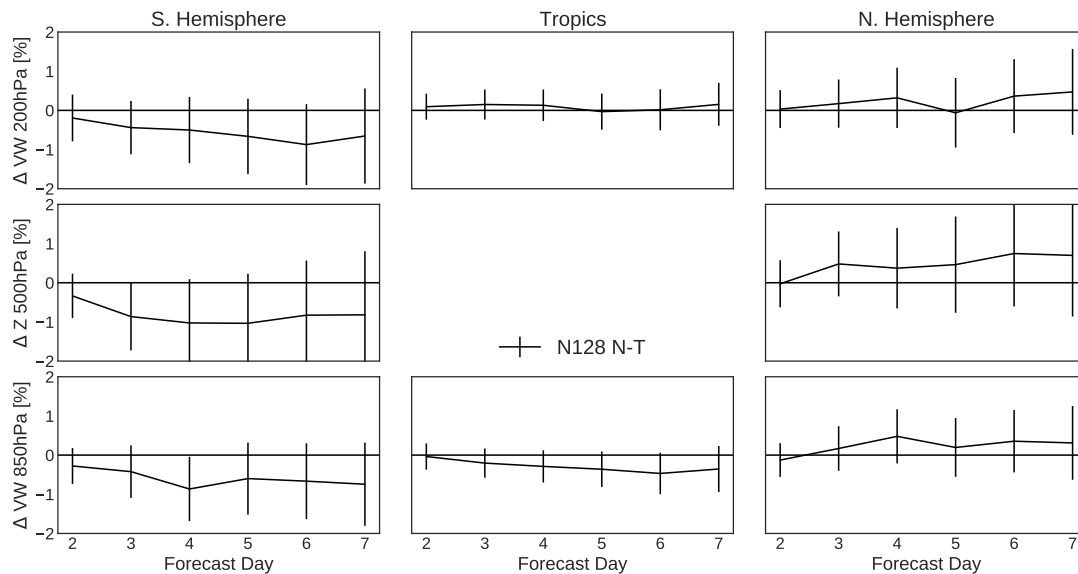
Figure 7: Forecast score changes for either vector winds (VW) or geopotential height (Z) RMSE at 200 (top), 500 (middle), and 850 hPa (bottom). The reference (0% line) is Control (48r1), with N128 N-T given by the black line. Verification is against own analysis with confidence intervals of 95% following Geer (2016) in the vertical lines.

reasoned that theoretical considerations should then guide the choice of superob size, with N128 being a compromise spatial resolution that was adequate for the scale of clouds in the operational model at that time while not overly increasing computational cost. Comparison with Fig. 10 shows that using a higher-resolution forecast model somewhat mitigates this mismatch between model and observations for strongly scattering scenes, but systematic cloud biases in the middle of the PDF are not impacted much by superobbing or model resolution.

Figure 9 shows the short-range forecast impact from superobbing H-sounder observations in isolation. This reveals a similar impact to that seen in Fig. 6 from doubling the radiances assimilated, but of a smaller magnitude. Both changes improve the short-range forecast's fit to humidity-sensitive observations such as other 183 GHz channels, and infrared channels on GEO and LEO platforms; fits to wind observations and radiosondes are neutral to slightly positive for superobbing but more positive for the thinning change. The magnitude of the improvement for humidity-sensitive channels is about half that of the data doubling, but this is still noteworthy as the only change here is averaging the radiances. It is logical to wonder what impact these two changes might have together when combined, and that is addressed in the next section. Medium-range forecast impacts from superobbing alone were entirely neutral in the experimentation, so no further figures are shown here.

A potential, intriguing side effect of superobbing H-sounder radiances may be increased impact from the 118 GHz channels on MWHS-2. These channels are limited in their influence due to high radiometric noise, and thus a significant decrease in the effective noise caused by superobbing (seen in Figs. 3 and 5) could permit greater impact on the analysis from these channels. To gauge this, we can look to observational fits for stratospheric observations, as these are pressure levels where 183 GHz channels have no direct sensitivity, although all-sky assimilation of tropospheric-sensitive radiances is well-known to increase gravity wave activity which can manifest in the stratosphere. However, all observational indicators are neutral above the tropopause, with no extra impact seen in radiosonde temperature, radio occultation, stratospheric AMSU-A channels, and so on. This is visible in Fig. 9, in that ATMS detects no improvement in std(O-B) for its stratospheric channels 10-15. We can revisit this question in Section A.2, where
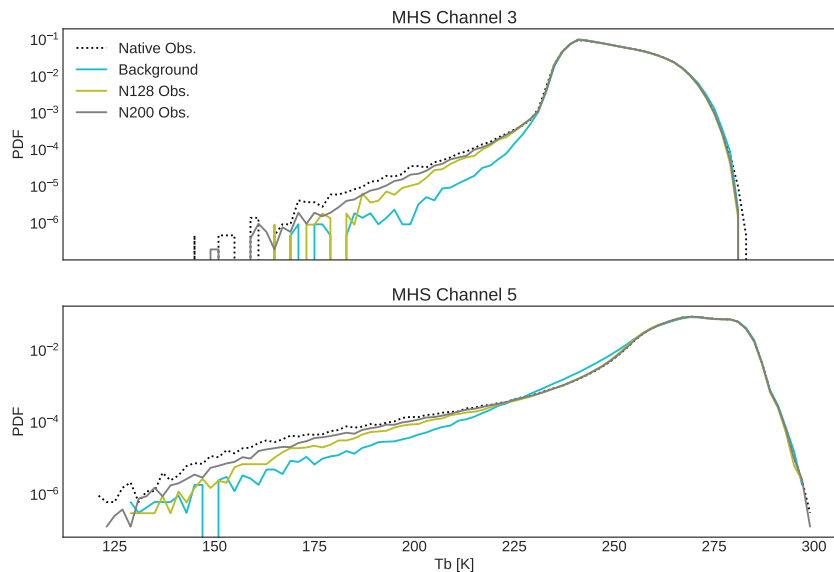
Figure 8: PDFs of MHS observations from channel 3 (top) and 5 (bottom) at native resolution and two superob resolutions as well as modelled radiances from the background (approximately 29 km model resolution). Data are limited to ice-free ocean scenes from Metop-B, Metop-C, and NOAA-19.

these channels receive more weight after having their observation errors adjusted.

3.2.2 Optimal Superob Resolution

Following the clear benefits of superobbing H-sounder radiances seen in the previous section, it is natural to consider whether some spatial resolution of averaging might be optimal. It is worth considering that the native resolution of H-sounders near their scan edge is considerably larger than at nadir, as large as 51 by 27 km for MHS at the maximum scan angle (Robel and Graumann, 2014) and larger still for the 118 GHz channels on MWHS-2. Thus superob resolutions that are finer than FOV size (at least for some scan positions) could be considered problematic. As discussed by Geer *et al.* (2017a), the ideal situation would be observations that match the "effective model resolution" so that representation error can be neglected. Effective model resolution is understood to be roughly 3 to 4 times the final model resolution when judged by kinetic energy spectra (Ricard *et al.*, 2013; Klaver *et al.*, 2020), in that modelled clouds and atmospheric waves remain larger than the grid spacing due to spectral filtering of small waves. Another possible solution is to "supermodel" the background field so that these realisations of the model fields match the resolution of the observations, but this has yet to be explored for the IFS (Geer *et al.*, 2017a).

To examine this, Fig. 10 shows the impact of model resolution on the PDF of background brightness temperatures, specifically for the current operational high-resolution version of the IFS, HRES at 9 km model resolution, against the resolution used in the experimentation presented here which uses 29 km model resolution. As we might expect, the higher-resolution model produces a slightly wider PDF of TBs, in particular a larger proportion of very strong scattering scenes. This resolution-dependence of how well the observations can match the model background is something to bear in mind when discussing experiments all run at the same model resolution.

A series of experiments were run (Table 4) in which the thinning was varied in tandem with the superob
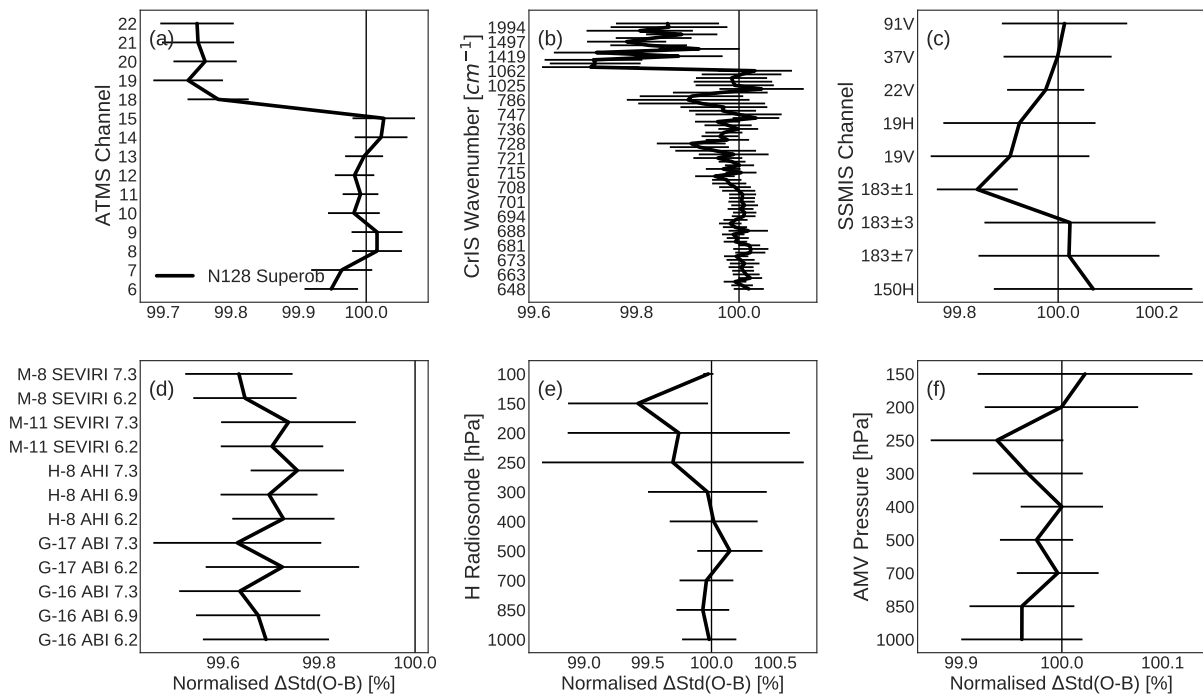
Figure 9: As Fig. 6 but showing the effect of superobbing alone.

resolution to largely conserve the volume of data assimilated, with superobs ranging from about 80 km to 40 km. This is intended to isolate the signal from the change in superob resolution. Hence in Fig. 11, the point of comparison, i.e. 100% line, is the N128 Superob experiment; in other words, we are testing on top of the result given in the previous section. Figure 11 shows that the choice of superob resolution has surprisingly little impact on the fits to independent observations, indicating that the superob resolution by itself is not a major factor in the quality of the short-range forecast, at least within the range of super-obbing scales considered. The only panel in Fig. 11 that appears noteworthy is a small degradation of fits to GEO infrared radiances, primarily those from Himawari-8. It is not clear why GEO infrared fits degrade slightly with finer H-sounder superobs. There is no systematic signal in the observational fits, whereas we might have expected some observation types to favour finer or coarser superobs. No forecast scores are shown here, as there were no significant impacts seen over two months of experimentation, with all scores looking neutral.

It may be significant for the interpretation of these results that all experimentation discussed is at TCo399 final model resolution. Would the conclusions change if these comparisons were done at the operational high-resolution model spacing of 9 km? This is beyond the scope of the current paper, but it is an important question and is intended for future investigation. If the above-mentioned theory of matching the model effective resolution is roughly correct, then a superob resolution of roughly 90 to 120 km would perform best for the model at TCo399, i.e. 3-4 times the model grid spacing. A finer superob resolution may be preferable for higher-resolution model grids, but this remains to be seen.

3.3   Superobbing and Finer Thinning

With the prior results showing the benefit of superobbing H-sounder radiances and increasing the volume of data assimilated, now we will assess the impact of these changes combined. As the sensitivity analysis
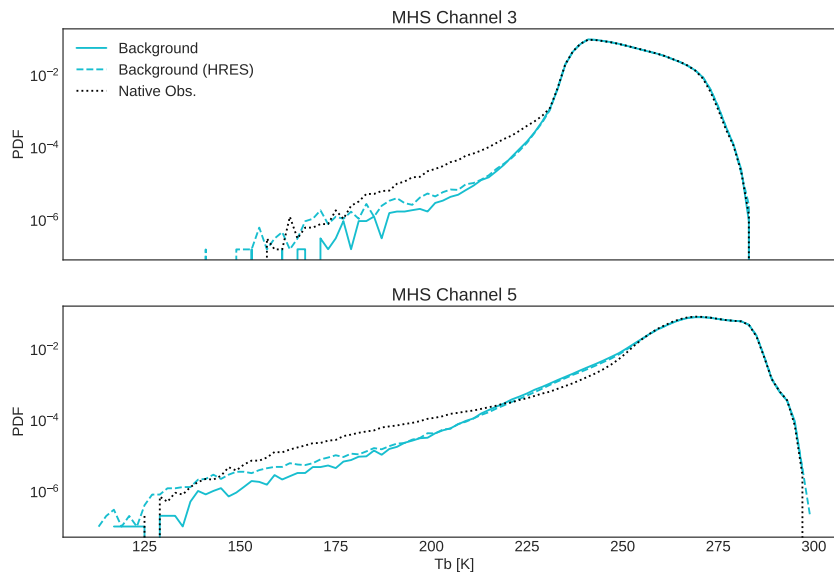
Figure 10: As Fig. 8 but PDFs of simulated radiances are shown from separate experiments producing the background at TCo399 (29 km) and TCo1279 (9 km; aka HRES) model resolution. Data here are from July 2020, compared to August 2021 in Fig. 8.

in Sec. 3.2.2 demonstrated, the results are almost entirely agnostic to the superob size, so here we use two different superob sizes more as a way to influence the eventual spacing. Comparing to the control, here we roughly double the data in the N128 Superob N-T experiment and add even more in the N200 Superob experiment, 137% more than in the control. This translates to the spacing of assimilated radiances going from roughly 110 km to about 80 and 70 km, respectively.

Figure 12 shows the change in background fits to other observations globally, again relative to the control. The signals here are familiar from earlier, with much-improved fits to humidity-sensitive observations especially. Again the impact on humidity is quite strong, with about a 1% decrease in std(O-B) for ATMS channels 19-22 and several IASI channels that is similar between the two experiments. Radiosonde observations of humidity and temperature indicate a small improvement in humidity at mid-levels and short-range temperature forecasts that are neutral to slightly improved. Radio occultation (RO) observations show a slight improvement in the UTLS, likely reflecting improved upper tropospheric humidity. The one observation type that shows a distinct difference between N128 and N200 is GEO infrared, which favours the larger N128 superobs; this is consistent with Fig. 11 where it was the only observation with sensitivity to superob size. Also as noted before, ATMS UTLS channels (8-10) show a minor degradation but this is not corroborated by RO, infrared, or radiosonde measurements. Overall, the results here appear as a combination of the results from previous sections.

To look in further detail at the impact on winds, Fig. 13 provides statistics from all wind-sensitive observations assimilated in the IFS. It shows that short-range, upper-tropospheric wind forecasts are improved slightly as seen in AMVs and Aeolus observations. The bottom row splits up conventional winds (i.e. radiosondes and wind profilers) to view the results regionally, as the addition of more H-sounder radiances elicits different impacts by region. In the Northern Hemisphere, winds in the upper troposphere (300-500 hPa) are improved. In the tropics, the effect is more concentrated near the tropopause (100-250 hPa) but quite significant. In the southern hemisphere there is little effect seen, however such observations are very sparse in this region. Lastly, the first panel in the figure gives various surface-sensitive observations. The satellite-based OSCAT and ASCAT scatterometers show small but significant improvements
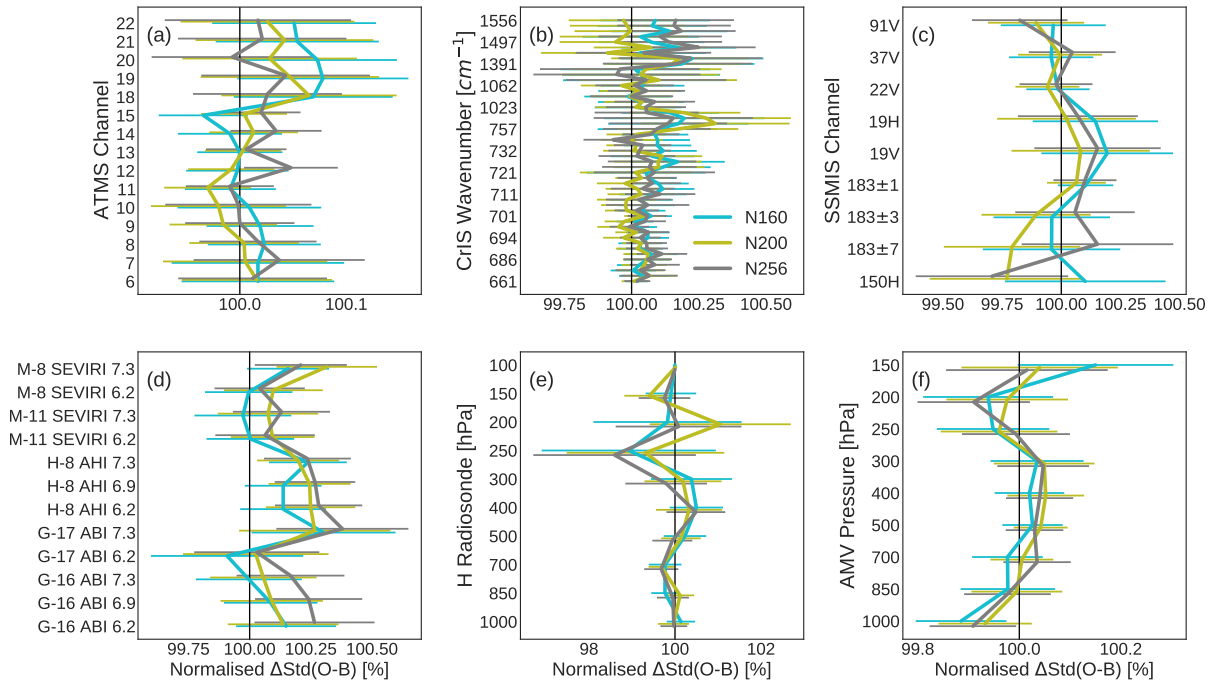
Figure 11: As Fig. 9 but with different superob resolutions compared against N128 Superob, i.e. 100% represents N128 Superob.

in std(O-B) due to the H-sounder changes, indicative of improved near-surface ocean winds, as do some surface pressure measurements. As with improved fit to AMVs at 1000 hPa, this indicates that impacts from adding H-sounder data are not limited to the upper troposphere.

To look at the impact on medium-range forecast scores, Fig. 14 provides the change in forecast RMSE for three pressure levels. This shows that despite the 6-month period of experimentation and the significant improvements seen in the short-range via fits to observations, there are not large impacts seen on the medium-range forecasts in these experiments. Mid- and lower-tropospheric forecasts appear improved in the Southern Hemisphere, with day-4 Southern Hemispheric winds on the verge of 95% confidence intervals at 850 hPa, but a longer period would be required to establish significant forecast impacts beyond doubt. There are not significant differences seen when comparing N128 Superob N-T and N200 Superob for medium-range forecast scores.

4   Conclusions

This study has examined the thinning and superobbing aspects of the all-sky assimilation of MW humidity sounder radiances in the IFS. In line with recent studies that have found benefits from additional microwave sounder data in the assimilation (Duncan *et al.*, 2021; Lean *et al.*, 2022), the addition of H-sounder data is shown to improve short-range forecasts of humidity and winds considerably. "Additional data" refers to less thinning of sounder radiances and also the change to superobbing of radiances, which effectively adds information by averaging together many radiances that were previously discarded. In combination, superobbing and using more finely-spaced H-sounder radiances appear as largely additive benefits for short-range forecasts, better constraining mid- to upper-tropospheric moisture and winds as seen by independent observations (compare black lines from Figs. 6 and 12). There are also some
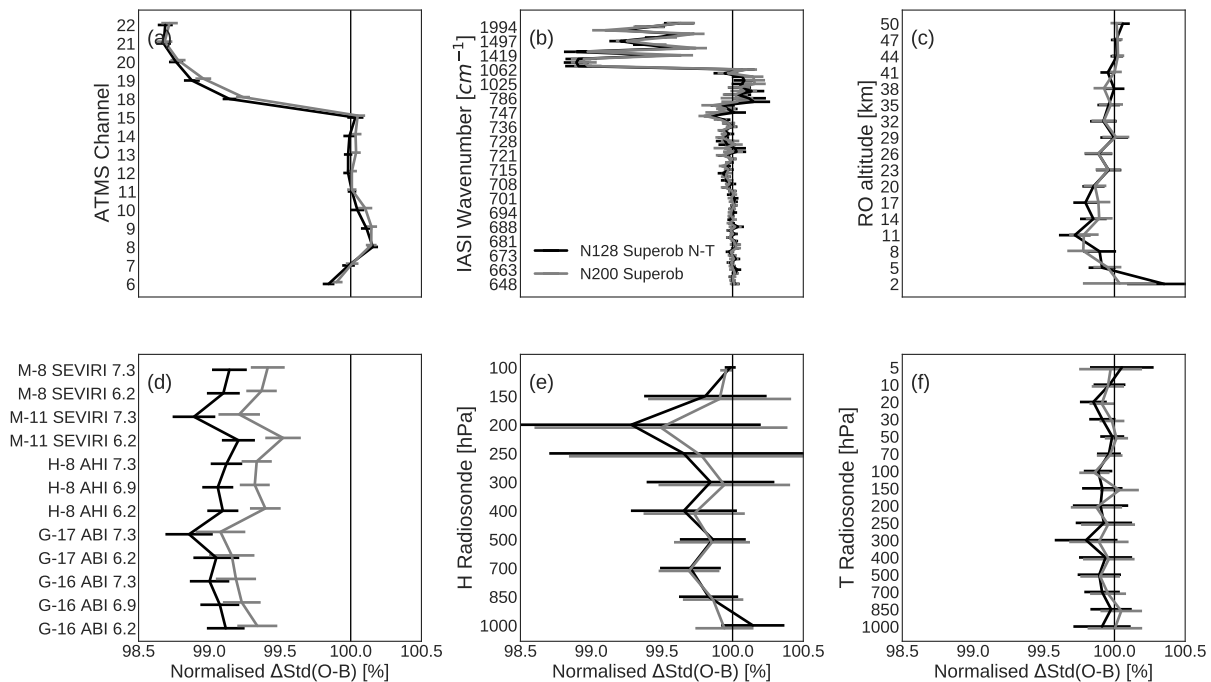
Figure 12: Change in std(O-B) for independent observations relative to 48r1 Control. These include global data from ATMS (a), IASI (b), GNSS radio occultation (c), GEO infrared (d), radiosonde humidity (e), and radiosonde temperature (f).

small benefits in the medium-range visible in the Southern Hemisphere. Such impacts are of a similar or larger magnitude than typically seen for a new microwave sensor activation in the IFS, underscoring the importance of the observation processing prior to assimilation.

The shift to using spatially-averaged H-sounder radiances is one that was foreseen by Geer *et al.* (2014), with this change by itself having a positive effect on the assimilation. More than a mere technical change to align the H-sounders' observation processing with the microwave imagers, superobbing leads to some clear improvements by itself (Fig. 9). The interpretation of this outcome is that superobbing acts to beat down the noise slightly and decrease representation error, while providing a smoother field of increments. It can also be considered a fuller use of each sensor's total information content.

Comparison of the thinning and superobbing results highlights that the addition of radiances is typically the dominant signal for NWP impact. Aspects such as averaging or observation error modelling also play a role, but the doubling of radiances caused by changing to a finer thinning scale was the largest signal in this set of experiments. This echoes findings from Duncan *et al.* (2021) and Duncan *et al.* (2022a), in that addition of data is the largest signal and elements such as the background errors or choice of observation error model are of secondary importance, albeit also crucial for an optimal assimilation. However, there are of course cases in which addition of observations degrades the analysis, such as with no thinning of radiances whatsoever. This type of analysis—to explore optimal thinning distances and pinpoint where spatial error correlations overwhelm the benefit of additional data a la Liu and Rabier (2002)—is the subject of a future study. The interplay between model resolution and optimal superob size was not investigated here but is also ripe for future analysis, as is possible interaction with the assimilation resolution itself (i.e. inner loop resolution). More benefit might be expected from a higher density of observations in a higher-resolution model, and this is intended for future investigation as well. Additional experimentation at 9km final model resolution (not shown) suggests that the impact of
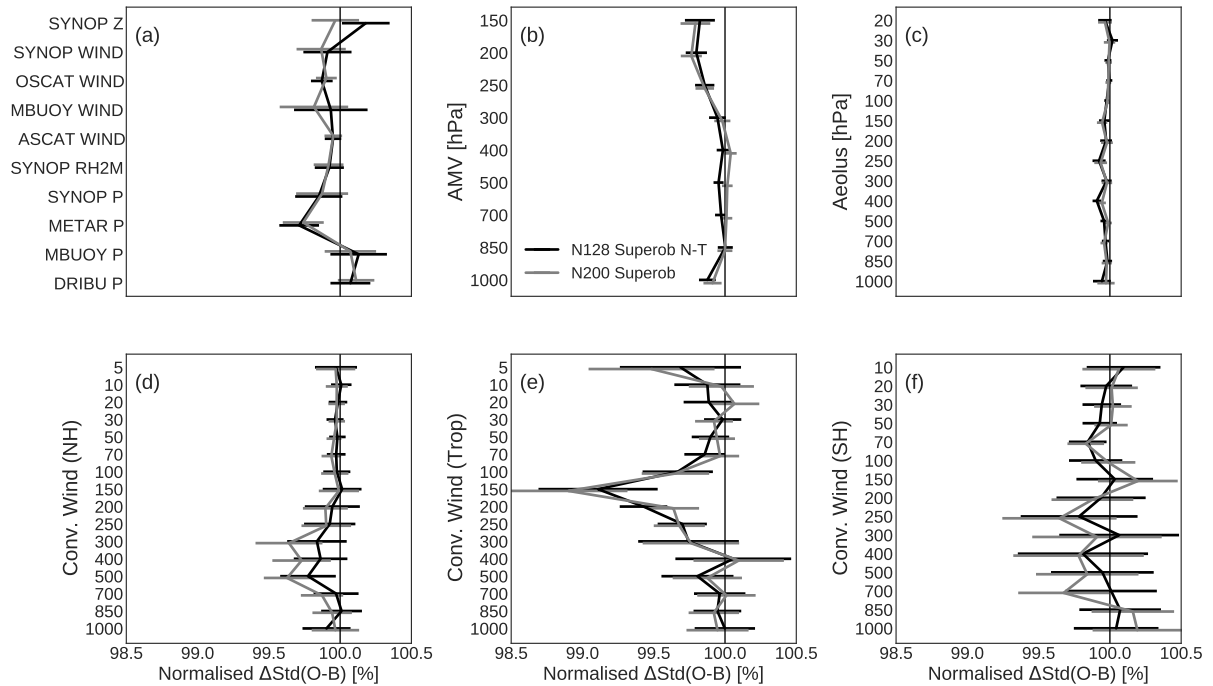
Figure 13: As Fig. 12 but focused on winds. The top row gives global statistics from surface-sensitive wind and pressure observations (a), AMVs (b), and Aeolus (c). The bottom row shows conventional wind observations (wind profilers and radiosonde-derived winds) split up into: (d) NH (20-90N), (e) tropics (20S-20N), and (f) SH (20-90S).

these changes is enhanced when a finer inner-loop resolution is used, and future experimentation will investigate this aspect more systematically.

An open question concerning the results presented is why the large improvements in fits to independent observations do not necessarily translate to improvements in medium-range forecast scores. A reasonable point of comparison is the assimilation of lidar wind retrievals from Aeolus (Rennie et al., 2021), which had a comparable impact on fits to observations in the IFS, but saw significant medium-range impact in UTLS temperatures and mid-tropospheric tropical winds especially. Two potential reasons are mentioned here. First, although fits to humidity-sensitive observations were significantly improved here, temperature-sensitive observations showed a more neutral impact, and if atmospheric mass is the primary conduit for transmitting longer-lived atmospheric patterns, this could explain the limited impact later in the forecast. Second, it is possible that heavier use of H-sounders largely adjusts the analysis to better fit inertia-gravity wave activity in the upper troposphere, but that this does not really benefit forecasts because the IFS cannot handle such waves sufficiently. It may be necessary to examine future results against a depleted observing system to shed more light on this connection between short-range humidity forecasts and the medium-range.

This study has demonstrated that all-sky assimilation of the MHS and MWHS-2 sensors in the IFS can be augmented in ways that significantly expand the benefits that they provide on the forecasts of moisture and winds. The optimal usage of observational data for NWP is impossible to define absolutely, as aspects such as model resolution have an effect and the global observing system is always changing; it is impossible to tune every aspect of the observation processing and assimilation in months-long experiments—parameter estimation is not suitable for this type of task. With this in mind, it is important to let physical intuition influence the decision-making as well. The results herein show unambiguously that superobbing is beneficial, as is decreased thinning of radiances. The superob size itself is relatively
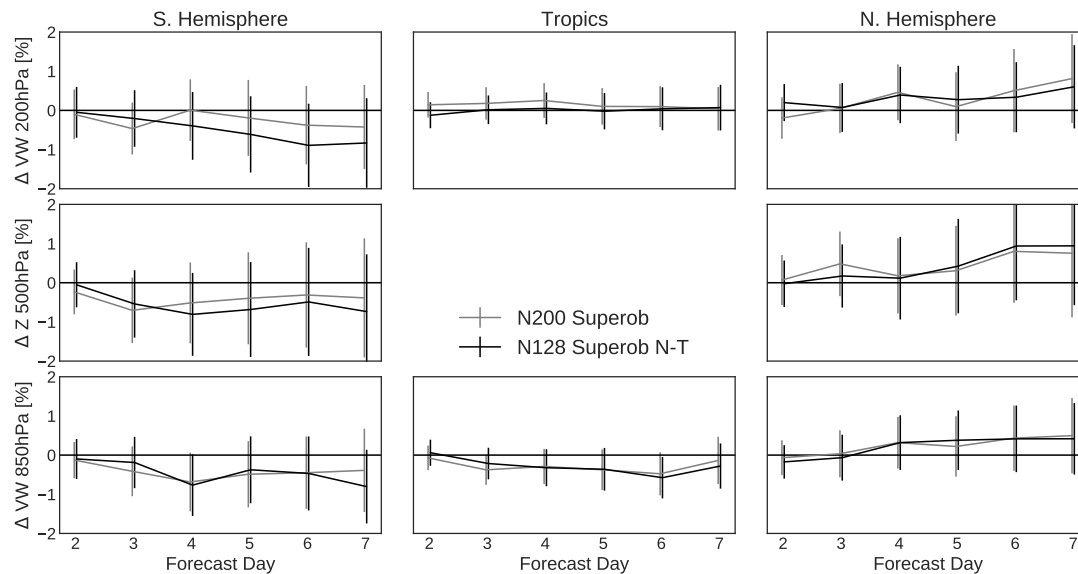
Figure 14: As Fig. 7 but with N128 Superob N-T given by the black line and N200 Superob in grey, with score changes in reference to Control (48r1).

unimportant, and changes to the observation error model need to be done carefully. Considering that the experimentation here was at 29 km resolution and NWP models march inexorably towards higher resolutions, it is reasonable to select the finest superob resolution tested here (50 km) to better align the processing of H-sounder radiances in the IFS with future increases of inner loop resolution as well as model resolution.

As a result of this study, the treatment of radiances from all-sky humidity sounders will change in IFS Cycle 49r1—this is illustrated in Fig. 15. MHS and MWHS-2 radiances will be superobbed to 50 km (N200) and thinned within the IFS to 70 km spacing. 118 GHz radiances from MWHS-2 undergo extra thinning to 100 km to avoid spatially correlated errors and more closely align their treatment with that of all-sky AMSU-A. This change leads to a significant increase in assimilated all-sky radiances in the IFS— 140% more from cross-track 183 GHz channels and 20% more from 118 GHz channels. Furthermore, the finer spacing of 50 km superobs permits 2.3 times more data through the screening trajectory, which should enable finer diagnostic analysis of small-scale features.
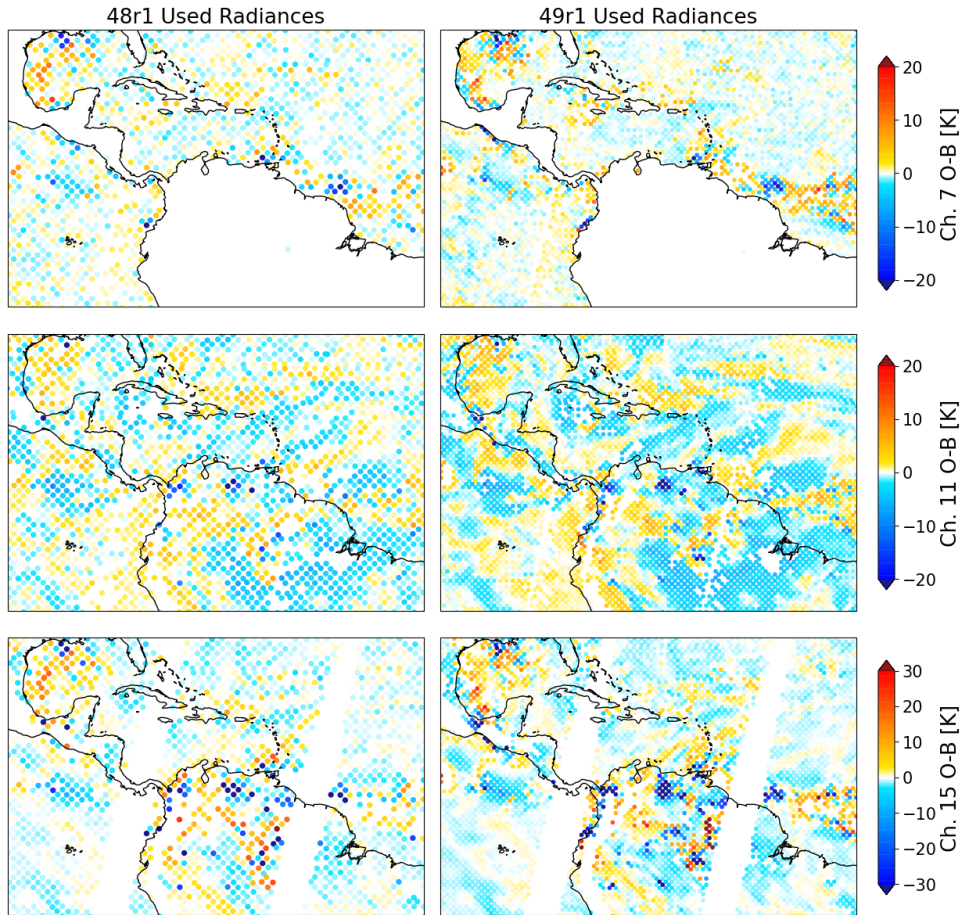
Figure 15: Observations minus background (O-B) over Central America from three channels on FY-3D MWHS-2: 7 (top), 11 (middle), 15 (bottom). The columns show assimilated radiances as used in Cycle 48r1 (native resolution thinned to 110km spacing) and Cycle 49r1 (50km superobs at 70km spacing). Data are from the 0Z long window on 5th June, 2021.

A   Appendix: Adjusted Observation Errors

A.1   Method

Here we test adjustments to the observation error model to account for the changed std(O-B) characteristics caused by superobbing. These changes include decreased errors of up to 10-25% at nadir for 183 GHz channels and 15-50% for 118 GHz channels, with larger decreases for higher-peaking channels. The other change is an augmentation of the all-sky error model that inflates the observation error as a function of zenith angle (θ) by dividing it by this function:

$$f(\theta) = 0.3 + 0.7 exp(-\frac{\beta^2 \theta^2}{2}) \qquad (2)$$

The error model value is scaled by $f(\theta)$ so that higher zenith angles receive less weight in the assimilation, with $\beta = 0.6$ and $\beta = 1.0$ for 183 and 118 GHz channels, respectively; these values lead to maximum error inflation of about 18% and 50% at MWHS-2 scan edge relative to nadir. Note that this

error scaling is the inverse of that applied for AMSU-A, where nadir-viewing observation errors are inflated due to greater surface and precipitation sensitivity caused by the higher atmospheric transmittance. Of the 118 GHz channels, only the higher-peaking ones (2-5) have this extra scaling applied, as channels 6 and 7 are affected by clouds at lower zenith angles and noise is less of a concern. The goal of all-sky error modelling is to smoothly assimilate radiances from clear skies to cloudy and precipitating scenes, ideally with normalised O-B statistics that are relatively uniform across various axes so that observations are not over- or under-weighted in the assimilation. Scaling observation errors using Eq. 2 is a method to ensure that radiances at higher zenith angles are not over-weighted relative to near-nadir radiances.
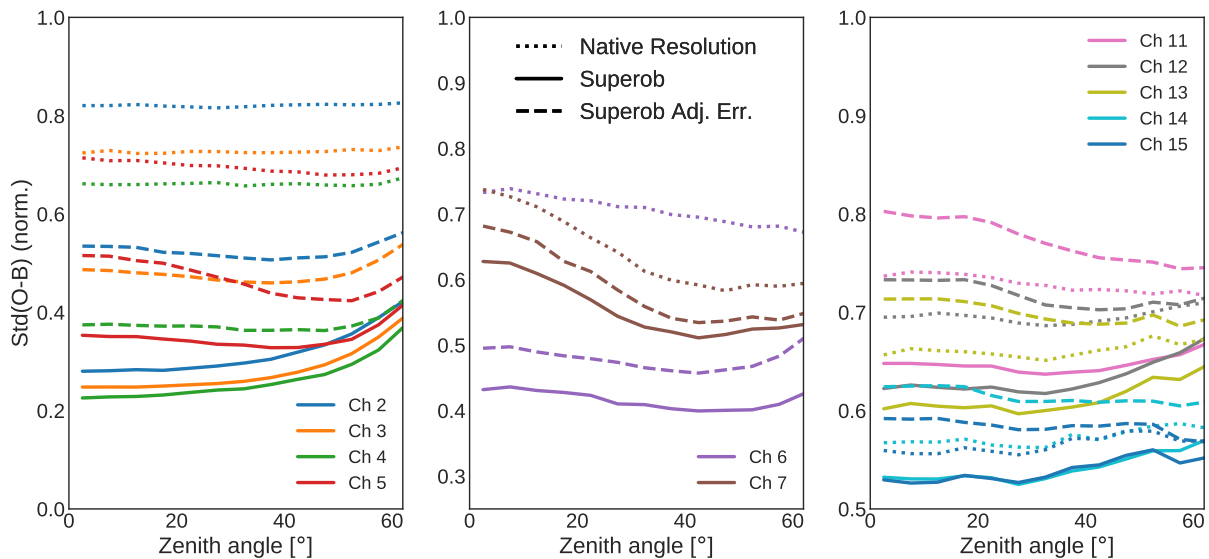

Figure 16: Same as Fig. 5 but with lines added for N128 superob with adjusted observation errors (dashed).

The dashed lines in Figure 16 encompass the two aforementioned adjustments to the error models—overall decrease in error values and inflation of errors at higher zenith angles. This appears moderately successful for channels 2-4 by increasing their weight slightly while largely keeping std(O-B) flat as a function of zenith angle. Channels 5-7 have more complex behaviour, and it is debatable whether these should have angle-dependent adjustments or not; indeed channel 7 may profit from the opposite zenith-based error adjustment (a la AMSU-A channel 5) regardless of the choice to superob. For the 183 GHz channels, the adjusted errors increase the weight of these observations relative to the control at native resolution by more than compensating for the effect of superob noise reduction. This may be acceptable because these channels' errors were conservative to begin with at around 0.6-0.7 normalised std(O-B). The un-adjusted (solid) lines have only a mild dependence on the zenith angle, and the adjusted error model somewhat overcompensates for this small effect at 183 GHz.

Without yet seeing assimilation results from these adjusted error experiments and purely judging by Fig. 16, it appears that using Eq. 2 to adjust the error model as a function of zenith angle is perhaps most justifiable for channels 2-4, and marginally so for higher-peaking 183 GHz channels like 11-13 on MWHS-2. Superobbing decreases std(O-B) more significantly for low zenith angles but it is a minor effect for most H-sounder channels considered. In fact, these plots make clear that a better zenith-based weighting of channel 7 may be more important for consistent departure statistics across the scan than small adjustments for the other channels. Otherwise, changes in the overall magnitude of errors can be said to still under-weight each 118 GHz channel relative to the control and give more weight to the 183 GHz channels. One could also consider other functions or tuning the beta value in Eq. 2 on a channel by channel basis to better suit the dependence on zenith angle seen here.
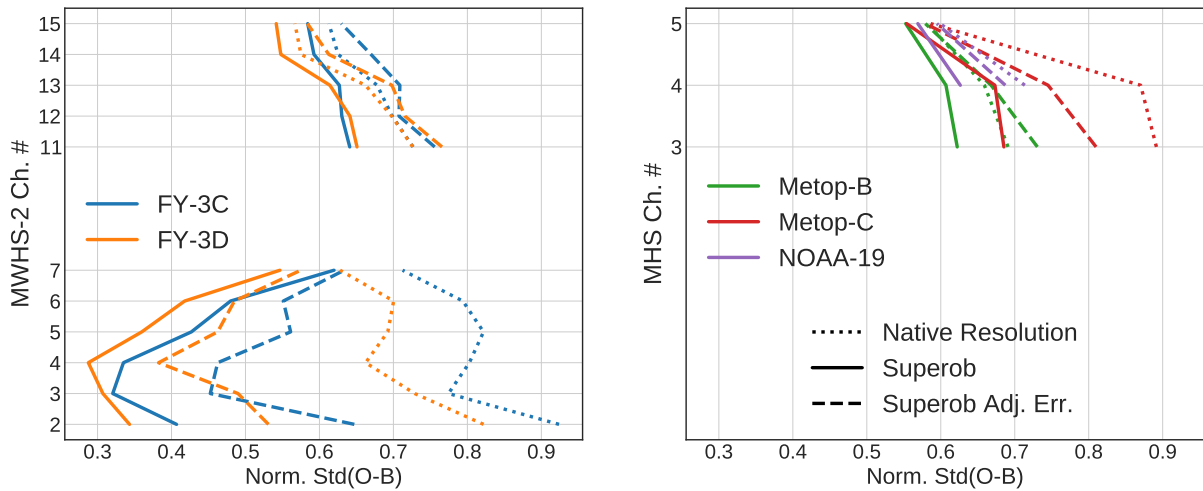
A.2   Results

Figure 17: Normalised std(O-B) for all active H-sounder channels. As Fig. 5 with experiments showing radiances used that are: native resolution (dotted), superobbed (solid), and superobbed with adjusted errors (dashed). Data span 1-10 August, 2021.

As described in Section 2.2, the move from native resolution to spatially-averaged radiances, i.e. super-obs, may prompt re-tuning the observation errors. To test this, we directly compare the N128 Superob N-T experiment from the previous section with an identical experiment where only the observation errors have changed. The effect of these adjustments to the observation errors assigned is seen in Fig. 17 for normalised std(O-B). After the adjustment of observation errors, normalised std(O-B) increases slightly for most channels and most markedly for 118 GHz channels. All H-sounder channels exhibit normalised std(O-B) significantly less than 1.0, as the adjustments err on the side of under-weighting rather than over-weighting the data. It is notable that most 118 GHz channels have low normalised values, near 0.5. For the most part, the assigned errors appear conservative in that normalised std(O-B) remains far less than 1.0. Most channels are still under-weighted relative to the experiment with un-averaged (i.e. native resolution) data, particularly for the 118 GHz channels.

Figure 18 shows the effect of re-tuning the observation error models for superobbed H-sounder radiances, as seen in short-range forecast fits to independent observations. In Fig. 18 the 100% line is the N128 Superob N-T experiment, so the signal is from the observation error adjustment alone. As in previous sections, fits to humidity-sensitive ATMS channels see further improvement when H-sounder radiances receive more weight in the assimilation. However, in this instance the degradation of ATMS 50 GHz fits is more pronounced and extends more broadly into the stratosphere (up to ATMS channel 13). This may indicate slight over-weighting of the 118 GHz channels on MWHS-2, perhaps due to unaccounted-for inter-channel or spatially-correlated error characteristics, which are possibly caused by the more pronounced "striping" evident after superobbing (Fig. 3). Hyperspectral infrared sounders witness a small but significant improvement in fit for some humidity channels, with temperature channels largely unaffected. In contrast, GEO infrared fits are largely neutral but with two channels slightly degraded. For winds, AMV fits appear neutral, as is Aeolus (not shown), whilst conventional winds indicate a small but significant improvement in the mid- to upper-tropospheric fits in the extra-tropics (not shown).

There are no medium-range forecast impacts from the adjusted observation errors alone that are statistically significant. But it may be worth considering this change on top of the superobbing and addition of data, comparing both against the control 48r1 experiment. Figure 19 provides the same view as Fig. 14
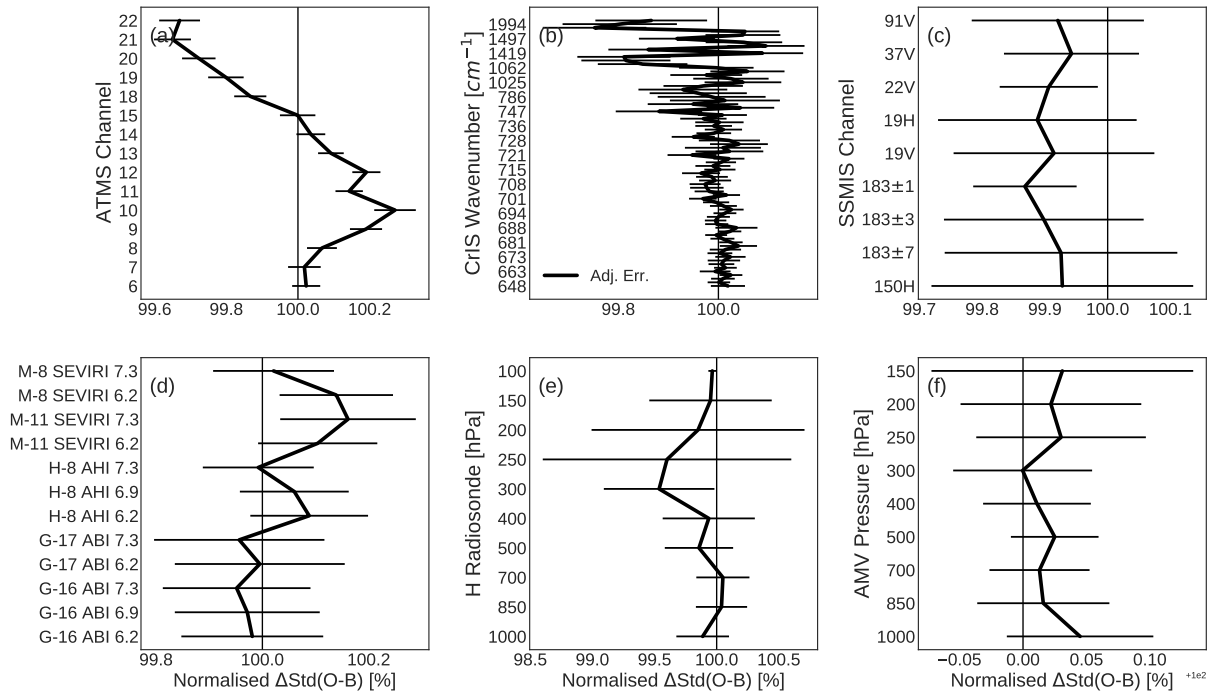
Figure 18: As Fig. 12 but for adjusted observation errors against the N128 Superob N-T as control. Global data are shown.

but shows the two N128 Superob N-T experiments side by side in comparison to the 48r1 control. In this view the adjusted observation errors show a small improvement in Southern Hemisphere forecast scores in the medium-range, just pushing some of these to statistical significance at the 95% confidence level at day 3. There does not appear to be much influence of the adjusted errors on medium-range scores elsewhere, though winds in the upper troposphere are slightly improved at day-2 in the Northern Hemisphere.

A.3 Conclusion

This was a speculative experiment and not set up methodically. The results suggest that there may be some benefit available from further tuning of observation error models for H-sounders, but that these need to be done carefully. The move to superobbing of H-sounder radiances in the IFS does not necessitate re-tuning of their observation errors. Other than the stratospheric 118 GHz channels, H-sounder radiances are not generally noise-limited and thus it is the systematic rather than the random errors that dominate the total observation error. It may be worthwhile to further explore the scan position aspect of the error model in the future; this is something already applied in the IFS for all-sky AMSU-A, and thus it might prove beneficial for low-peaking 118 GHz channels (especially the lower-noise channels on FY-3E). However, tighter observation error modelling may expose the assimilation system more to systematic errors such as striping from the sensor or correlated observation errors (spatial or inter-channel), and either of these may be more pressing to address for optimisation of H-sounder assimilation.

The changes tested in Sec. A.2 suggest some improvements from applying tighter errors to the 183 GHz channels, but tighter errors on 118 GHz channels seemed to give these channels more weight than optimal in the assimilation. However, this argument is quite implicit, and further investigation would
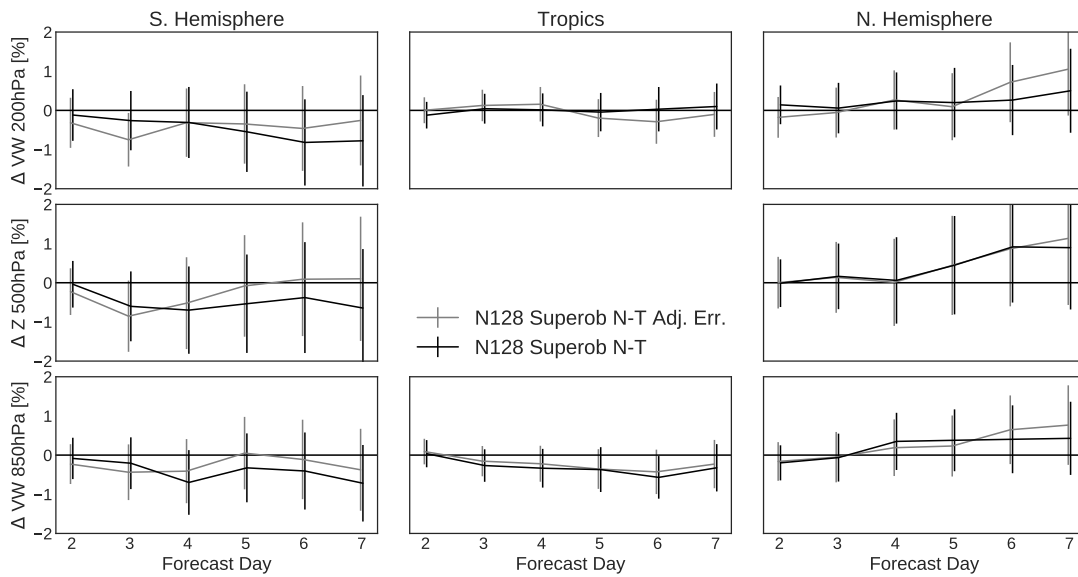
Figure 19: As Fig. 14 but comparing experiments with and without adjusted observation errors. Again the black line shows N128 Superob N-T, with the grey line now N128 Superob N-T with adjusted observation errors.

be required to identify whether inter-channel or spatial error correlations may be to blame. It is quite plausible that an optimal thinning resolution for H-sounder radiances is different for low-peaking 183 GHz channels and stratospheric 118 GHz channels; considering the current thinning scales for AMSU-A and ATMS radiances in the IFS—about 125 km—it is unsurprising that the 118 GHz channels require very conservative observation errors at finer thinning scales to combat spatially correlated errors. It may be worth testing separate thinning scales for the 118 and 183 GHz channels on MWHS-2 in the future, perhaps simply by retaining secondary (i.e. within IFS) thinning for temperature sounding channels. This may also be an important consideration for future assimilation of mixed sensors like ATMS in the all-sky system.

Acknowledgements

Glossary

4D-Var Four-dimensional variational data assimilation. 8

AMSU-A Advanced Microwave Sounding Unit-A. 2

ATMS Advanced Technology Microwave Sounder. 1

EDA Ensemble of data assimilations. 8

FOV Field of view (instantaneous). 2

GEO Geostationary orbit. 10

GMI Global Precipitation Measurement (GPM) Microwave Imager. 1

IFS Integrated Forecasting System. 1

ITCZ Intertropical Convergence Zone. 5

LEO Low Earth orbit. 2

MHS Microwave Humidity Sounder. 1

MWHS-2 MicroWave Humidity Sounder 2. 1

NEDT Noise equivalent differential temperature. 2

NWP Numerical weather prediction. 2

PDF Probability Density Function. 11

RTTOV-SCATT Radiative transfer for TOVS microwave scattering package. 6

SI Scattering index. 8

SSMIS Special Sensor Microwave Imager Sounder. 1

Tb Brightness temperature. 8, 11

UTLS Upper troposphere / lower stratosphere. 10

References

Bédard, J. and Buehner, M. (2020). A practical assimilation approach to extract smaller-scale information from observations with spatially correlated errors: An idealized study. *Quart. J. Roy. Meteor. Soc.*, **146**(726), 468–482, doi:https://doi.org/10.1002/qj.3687, URL https://rmets.onlinelibrary.wiley.com/doi/abs/10.1002/qj.3687.

Bennartz, R. (2000). Optimal convolution of AMSU-B to AMSU-A. *J. Atmos. Oceanic Technol.*, **17**(9), 1215–1225, doi:10.1175/1520-0426(2000)017⟨1215:OCOABT⟩2.0.CO;2.

Bergman, K. H. and Bonner, W. D. (1976). Analysis error as a function of observation density for satellite temperature soundings with spatially correlated errors. *Mon. Weather Rev.*, **104**(10), 1308 – 1316, doi:10.1175/1520-0493(1976)104⟨1308:AEAAFO⟩2.0.CO;2, URL https://journals.ametsoc.org/view/journals/mwre/104/10/1520-0493_1976_104_1308_aeaafo_2_0_co_2.xml.

Bonavita, M., Geer, A. J. and Hamrud, M. (2020). All-sky microwave radiances assimilated with an ensemble Kalman filter. *Mon. Weather Rev.*, **148**(7), 2737 – 2760, doi:10.1175/MWR-D-19-0413.1, URL https://journals.ametsoc.org/view/journals/mwre/148/7/mwrD190413.xml.

Bormann, N. (2017). Slant path radiative transfer for the assimilation of sounder radiances. *Tellus A*, **69**(1), 1272779, doi:10.1080/16000870.2016.1272779, URL https://doi.org/10.1080/16000870.2016.1272779.

Bormann, N. and Bauer, P. (2010). Estimates of spatial and interchannel observation-error characteristics for current sounder radiances for numerical weather prediction. I: Methods and application to ATOVS data. *Quart. J. Roy. Meteor. Soc.*, **136**(649), 1036–1050, doi:10.1002/qj.616, URL https://rmets.onlinelibrary.wiley.com/doi/abs/10.1002/qj.616.

Bormann, N., Duncan, D., English, S., Healy, S., Lonitz, K., Chen, K., Lawrence, H. and Lu, Q. (2021). Growing operational use of FY-3 data in the ECMWF system. *Adv. Atmos. Sci.*, doi:10.1007/s00376-020-0207-3, URL https://doi.org/10.1007/s00376-020-0207-3.

Candy, B. and Migliorini, S. (2021). The assimilation of microwave humidity sounder observations in all-sky conditions. *Quart. J. Roy. Meteor. Soc.*, **147**(739), 3049–3066, doi:https://doi.org/10.1002/qj.4115, URL https://rmets.onlinelibrary.wiley.com/doi/abs/10.1002/qj.4115.

Carminati, F. and Migliorini, S. (2021). All-sky data assimilation of MWTS-2 and MWHS-2 in the Met Office global NWP system. *Adv. Atmos. Sci.*, **38**(10), 1682–1694, doi:10.1007/s00376-021-1071-5, URL https://doi.org/10.1007/s00376-021-1071-5.

Dando, M. L., Thorpe, A. J. and Eyre, J. R. (2007). The optimal density of atmospheric sounder observations in the Met Office NWP system. *Quart. J. Roy. Meteor. Soc.*, **133**(629), 1933–1943, doi:https://doi.org/10.1002/qj.175, URL https://rmets.onlinelibrary.wiley.com/doi/abs/10.1002/qj.175.

Duncan, D. and Bormann, N. (2020). On the addition of microwave sounders and NWP skill, including assessment of FY-3D sounders. *Technical Report 55*, EUMETSAT/ECMWF Fellowship Programme Research Report, doi:10.21957/iimhohmqt, URL https://www.ecmwf.int/node/19760.

Duncan, D. I., Bormann, N. and Geer, A. J. (2022a). All-sky assimilation of AMSU-A window channels. *Technical Report 59*, EUMETSAT/ECMWF Fellowship Programme Research Report, Shinfield Park, Reading, doi:10.21957/daefm16p8, URL https://www.ecmwf.int/node/20457.

Duncan, D. I., Bormann, N., Geer, A. J. and Weston, P. (2022b). Assimilation of AMSU-A in all-sky conditions. *Mon. Weather Rev.*, **150**(5), 1023 – 1041, doi:10.1175/MWR-D-21-0273.1, URL https://doi.org/10.1175/MWR-D-21-0273.1.

Duncan, D. I., Bormann, N. and Hólm, E. (2021). On the addition of microwave sounders and numerical weather prediction skill. *Quart. J. Roy. Meteor. Soc.*, **147**(740), 3703–3718, doi:10.1002/qj.4149, URL https://doi.org/10.1002/qj.4149.

Geer, A. J. (2016). Significance of changes in medium-range forecast scores. *Tellus A*, **68**(1), 30229, doi:10.3402/tellusa.v68.30229, URL https://doi.org/10.3402/tellusa.v68.30229.

Geer, A. J. (2021). Physical characteristics of frozen hydrometeors inferred with parameter estimation. *Atmos. Meas. Tech.*, **14**(8), 5369–5395, doi:10.5194/amt-14-5369-2021, URL https://doi.org/10.5194/amt-14-5369-2021.

Geer, A. J., Ahlgrimm, M., Bechtold, P., Bonavita, M., Bormann, N., English, S., Fielding, M., Forbes, R., Hogan, R., Hólm, E., Janiskova, M., Lonitz, K., Lopez, P., Matricardi, M., Sandu, I. and Weston, P. (2017a). Assimilating observations sensitive to cloud and precipitation. *Technical Report 815*, ECMWF Tech. Memo., Shinfield Park, Reading, doi:10.21957/sz7cr1dym, URL https://www.ecmwf.int/node/17718.

Geer, A. J., Baordo, F., Bormann, N., Chambon, P., English, S. J., Kazumori, M., Lawrence, H., Lean, P., Lonitz, K. and Lupu, C. (2017b). The growing impact of satellite observations sensitive to humidity, cloud and precipitation. *Quart. J. Roy. Meteor. Soc.*, **143**(709), 3189–3206, doi:10.1002/qj.3172, URL https://rmets.onlinelibrary.wiley.com/doi/abs/10.1002/qj.3172.

Geer, A. J., Baordo, F., Bormann, N. and English, S. (2014). All-sky assimilation of microwave humidity sounders. *Technical Report 741*, ECMWF Tech. Memo., doi:10.21957/obosmx154, URL https://www.ecmwf.int/node/9507.

Geer, A. J. and Bauer, P. (2010). Enhanced use of all-sky microwave observations sensitive to water vapour, cloud and precipitation. *Technical Report 20*, EUMETSAT/ECMWF Fellowship Programme Research Report, URL https://www.ecmwf.int/node/9506, also published as ECMWF Technical Memorandum No.620.

Geer, A. J. and Bauer, P. (2011). Observation errors in all-sky data assimilation. *Quart. J. Roy. Meteor. Soc.*, **137**(661), 2024–2037, doi:10.1002/qj.830, URL https://rmets.onlinelibrary.wiley.com/doi/abs/10.1002/qj.830.

Geer, A. J., Bauer, P., Lonitz, K., Barlakas, V., Eriksson, P., Mendrok, J., Doherty, A., Hocking, J. and Chambon, P. (2021). Bulk hydrometeor optical properties for microwave and sub-millimetre radiative transfer in RTTOV-SCATT v13.0. *Geosci. Model Dev.*, **14**(12), 7497–7526, doi:10.5194/gmd-14-7497-2021, URL https://gmd.copernicus.org/articles/14/7497/2021/.

Geer, A. J., Lonitz, K., Duncan, D. I. and Bormann, N. (2022). Improved surface treatment for all-sky microwave observations. *Technical Report 894*, ECMWF Tech. Memo., Shinfield Park, Reading, doi:10.21957/zi7q6hau, URL https://www.ecmwf.int/node/20337.

He, J., Zhang, S. and Wang, Z. (2014). Advanced microwave atmospheric sounder (AMAS) channel specifications and T/V calibration results on FY-3C satellite. *IEEE T. Geosci. Remote Sens.*, **53**(1), 481–493, doi:10.1109/TGRS.2014.2324173, URL dx.doi.org/10.1109/TGRS.2014.2324173.

Hoffman, R. N. (2018). The effect of thinning and superobservations in a simple one-dimensional data analysis with mischaracterized error. *Mon. Weather Rev.*, **146**(4), 1181 – 1195, doi:10.1175/MWR-D-17-0363.1, URL https://journals.ametsoc.org/view/journals/mwre/146/4/mwr-d-17-0363.1.xml.

Kim, M.-J., Jin, J., Akkraoui, A. E., McCarty, W., Todling, R., Gu, W. and Gelaro, R. (2020). The framework for assimilating all-sky GPM microwave imager brightness temperature data in the NASA GEOS data assimilation system. *Mon. Weather Rev.*, **148**(6), 2433 – 2455, doi:10.1175/MWR-D-19-0100.1, URL https://journals.ametsoc.org/view/journals/mwre/148/6/mwrD190100.xml.

Klaver, R., Haarsma, R., Vidale, P. L. and Hazeleger, W. (2020). Effective resolution in high resolution global atmospheric models for climate studies. *Atmos. Sci. Lett.*, **21**(4), e952, doi:https://doi.org/10.1002/asl.952, URL https://rmets.onlinelibrary.wiley.com/doi/abs/10.1002/asl.952.

Lawrence, H., Bormann, N., Geer, A. J., Lu, Q. and English, S. J. (2018). Evaluation and assimilation of the microwave sounder MWHS-2 onboard FY-3C in the ECMWF numerical weather prediction system. *IEEE T. Geosci. Remote Sens.*, **56**(6), 3333–3349, doi:10.1109/TGRS.2018.2798292, URL https://doi.org/10.1109/TGRS.2018.2798292.

Lean, K., Bormann, N. and Healy, S. (2022). Calibration of EDA spread and adaptation of the observation error model. *Technical Report WP-2000*, ECMWF, doi:10.21957/1auh0nztg, URL https://www.ecmwf.int/node/20302.

Liu, Z.-Q. and Rabier, F. (2002). The interaction between model resolution, observation resolution and observation density in data assimilation: A one-dimensional study. *Quart. J. Roy. Meteor. Soc.*, **128**(582), 1367–1386, doi:https://doi.org/10.1256/003590002320373337, URL https://rmets.onlinelibrary.wiley.com/doi/abs/10.1256/003590002320373337.

Maddy, E. S., Bunin, S., Mikles, V. J., Shahroudi, N., Shiotani, B. and Boukabara, S.-A. (2022). Temperature and moisture sounding performance of current and prospective microwave instruments under all-sky conditions. *Remote Sens.*, **14**(7), doi:10.3390/rs14071624, URL https://www.mdpi.com/2072-4292/14/7/1624.

O'Sullivan, D. and Dunkerton, T. J. (1995). Generation of inertia–gravity waves in a simulated life cycle of baroclinic instability. *J. Atmos. Sci.*, **52**(21), 3695 – 3716, doi:10.1175/1520-0469(1995)052⟨3695:GOIWIA⟩2.0.CO;2, URL https://journals.ametsoc.org/view/journals/atsc/52/21/1520-0469_1995_052_3695_goiwia_2_0_co_2.xml.

Peubey, C. and McNally, A. (2009). Characterization of the impact of geostationary clear-sky radiances on wind analyses in a 4D-Var context. *Quart. J. Roy. Meteor. Soc.*, **135**(644), 1863–1876, doi:10.1002/qj.500, URL https://rmets.onlinelibrary.wiley.com/doi/abs/10.1002/qj.500.

Rennie, M. P., Isaksen, L., Weiler, F., de Kloe, J., Kanitz, T. and Reitebuch, O. (2021). The impact of aeolus wind retrievals on ECMWF global weather forecasts. *Quart. J. Roy. Meteor. Soc.*, **147**(740), 3555–3586, doi:https://doi.org/10.1002/qj.4142, URL https://rmets.onlinelibrary.wiley.com/doi/abs/10.1002/qj.4142.

Ricard, D., Lac, C., Riette, S., Legrand, R. and Mary, A. (2013). Kinetic energy spectra characteristics of two convection-permitting limited-area models AROME and Meso-NH. *Quart. J. Roy. Meteor. Soc.*, **139**(674), 1327–1341, doi:https://doi.org/10.1002/qj.2025, URL https://rmets.onlinelibrary.wiley.com/doi/abs/10.1002/qj.2025.

Robel, J. and Graumann, A. (2014). NOAA KLM user's guide with NOAA-N, N Prime, and MetOp supplements. *Technical report*, NOAA NESDIS, URL https://lccn.loc.gov/2009578433.